# Evaporation and wetting behavior of silver-graphene hybrid nanofluid droplet on its porous residue surface for various mixing ratios

F.R. Siddiqui[1], C.Y. Tso[2], S.C. Fu[3], H.H. Qiu[1], Christopher Y. H. Chao[3*]

[1]Department of Mechanical and Aerospace Engineering, The Hong Kong University of Science and Technology, Hong Kong

[2]School of Energy and Environment, City University of Hong Kong, Hong Kong

[3]Department of Mechanical Engineering, The University of Hong Kong, Hong Kong

* Corresponding Author Tel.: +852 3917 2800

E-mail Address: cyhchao@hku.hk

Postal Address: Department of Mechanical Engineering, The University of Hong Kong, Pokfulam Road, Hong Kong

**Abstract**

Droplet evaporation has a high heat removal capacity and widely used in the form of spray cooling or dropwise cooling of various heat dissipating devices. However, due to the limiting heat flux removal capacity of conventional fluids, such as water, these cannot be used in thermal management of high heat flux devices. In this research, the evaporation of silver (Ag)-graphene (GNP) hybrid nanofluid droplet and its residue effects on the evaporation of subsequent Ag-GNP hybrid nanofluid droplet, due to its synergistic thermal properties, is experimentally investigated for various mixing ratios, from MR-1 (0.1(Ag):0.9(GNP)) to MR-5 (0.9(Ag):0.1(GNP)), and different residue sizes. A theoretical model is also proposed for hybrid nanofluid droplet evaporation and semi-empirical relations are developed to estimate the hybrid nanofluid droplet spreading over its residue surface. The results show a substantial increase in the droplet evaporation rate with increasing residue size and decreasing mixing ratio. MR-1 hybrid nanofluid droplet gives the highest evaporation rate (up to 370%) on its highly wetted residue surface, while the evaporation rate significantly drops moving from MR-2 to MR-5 hybrid nanofluid droplets on their partially wetted residue surfaces. Moreover, the evaporation rate substantially increases (up to 240%) with increasing residue size for MR-1 hybrid nanofluid droplet resting on its residue

31 <mark>surface, however, the effect of residue size on droplet evaporation rate considerably diminishes</mark>

32 <mark>moving from MR-2 to MR-5 hybrid nanofluid droplets resting on their respective residues.</mark>

33 **Keywords:** Droplet evaporation; wetting; hybrid nanofluid; porous residue; droplet spreading.

34

35 **Nomenclature**

| | | | |
|---|---|---|---|
| $A_s$ | Droplet surface area, m$^2$ | $V_{sd}$ | Volume of second droplet, µl |
| $a_p$ | Areal porosity | $V_{as}$ | Droplet volume above residue surface, µl |
| $C$ | Total molar concentration, kmolm$^{-3}$ | $V_{bs}$ | Droplet volume below residue surface, µl |
| $D$ | Mass diffusivity, m$^2$s$^{-1}$ | $V_{net}$ | Net droplet volume, µl |
| $\dot{E}_{ins}$ | Instantaneous evaporation rate, µls$^{-1}$ | $x_v$ | Vapor mole fraction |
| $\dot{E}_{net}$ | Net evaporation rate, µls$^{-1}$ | **Greek Letters** | |
| $\dot{E}''_{ins}$ | Instantaneous evaporation flux, µls$^{-1}$m$^{-2}$ | $\rho$ | Density, kgm$^{-3}$ |
| $g$ | Gravitational constant, ms$^{-2}$ | $\gamma_{lv}$ | Droplet surface tension, mNm$^{-1}$ |
| $h$ | Height, m | $\gamma_{sv}$ | Surface free energy, mNm$^{-1}$ |
| $h_c$ | Characteristic height, m | $\gamma_{sl}$ | <mark>Solid-liquid</mark> interfacial tension, mNm$^{-1}$ |
| $l_{ca}$ | Capillary length, m | $\varphi$ | Relative humidity |
| $M$ | Molar mass, g/mol | $\theta_{qe}$ | Quasi-equilibrium contact angle |
| $MR$ | Mixing ratio | $\theta_d$ | Dynamic contact angle |
| $P_a$ | Ambient Pressure, Pa | $\theta_s$ | Static contact angle |
| $P_{v,sat}$ | Saturation vapor pressure, Pa | $\theta_y$ | Young contact angle |
| $r$ | Roughness ratio | $\theta_a$ | Apparent contact angle |
| $R_a$ | Average surface roughness, µm | $\emptyset_{qe}$ | Quasi-equilibrium contact diameter, m |
| $R$ | Universal gas constant, Jmol$^{-1}$K$^{-1}$ | $\emptyset_d$ | Dynamic contact diameter, m |
| $T$ | Temperature, K | $\emptyset_s$ | Static contact diameter, m |
| $t$ | Time, s | $\emptyset_f$ | Mean Feret diameter, m |
| $VES$ | Vapor equilibrium surface | $\tau$ | Droplet spreading time scale, s |
| $V_{fd}$ | Volume of first droplet, µl | $\mu$ | Viscosity, Pas |

## 1. Introduction

Droplet evaporation is a universal phenomenon and finds a range of engineering applications such as spray cooling, printing, spray painting, fuel injection, and hotspot cooling in microelectronics. It is a phase change process with higher heat transfer rates as compared to the single-phase heat transfer processes. The evaporating droplet removes heat by utilizing the latent energy of its molecules until it transforms into a vapor. Despite all these advantages, thermal management of high heat flux devices ($10^6$-$10^7$ W/m$^2$) [1] is increasingly becoming a challenge thus limiting the use of conventional fluids (such as water) for such applications. Therefore, advanced thermal fluids, such as nanofluids with high heat removal capacity, are needed to address such challenges.

Nanofluid is the dispersion of very fine nano-sized particles in the base fluid (such as water), which substantially improves its thermal properties and is widely reported by researchers [2–4]. However, nanofluids do not possess overall hydrothermal properties, such as high stability and high thermal conductivity. For instance, metal (such as copper) nanofluids show high thermal conductivity but poor dispersion stability. On the other hand, metal-oxide (such as $Al_2O_3$) nanofluids exhibit high dispersion stability but low thermal conductivity. Due to this reason, single particle nanofluids are not suitable for heat transfer applications as they do not possess overall hydrothermal characteristics [5]. Recently, another class of nanofluid (known as the hybrid nanofluid) is investigated, which has resulted in better overall hydrothermal properties and is prepared by dispersing two different nanoparticle types (metal, metal-oxide or non-metal) in the base fluid. Also, the presence of two different nanoparticle types has a synergistic thermal effect, thus making the hybrid nanofluid a highly conductive fluid, which is not the case with single particle nanofluid. At even low particle concentration, hybrid nanofluids are reported to exhibit higher thermal conductivity than single particle nanofluids [6–9]. The synergistic thermal conductivity in the hybrid nanofluid is due to a thermal pathway created by one nanoparticle type with another nanoparticle type, thus reducing the overall thermal contact resistance between the nanoparticles and the surrounding molecules of the base fluid [10]. For this reason, the synergistic thermal effect in hybrid nanofluid highly depends on the inter-particle compatibility. It is the synergistically advanced thermal properties of the hybrid nanofluid that makes it a suitable candidate for thermal management of high heat flux applications.

The application of hybrid nanofluid in a phase change process, such as droplet evaporation, may result in a high heat removal rate and keep the surface temperatures within safe levels. There are several parameters that affect the evaporation rate of a sessile droplet such as the surface temperature, humidity, surface roughness and droplet surface tension, to name a few [11–13]. Besides, the droplet pinning or de-pinning effect over the substrate also affects its evaporation rate [14,15]. As reported by many researchers, the suspended nanoparticles in the nanofluid droplet migrate towards the edge and deposit near the three-phase contact line, which results in a droplet pinning effect during the evaporation process [16–21]. Other factors, such as the droplet contact angle, viscosity, and suspended nanoparticle type and concentration also influence the droplet evaporation rate [22–25]. Approximate solutions have also been developed to predict the evaporation rate of sessile droplets [26–28]. Moreover, the suspended nanoparticles in the sessile nanofluid/hybrid nanofluid droplet do not apparently improve the evaporation process, when all the three phases (droplet, solid substrate and the air) are in thermal equilibrium [14,21].

During evaporation, the concentration of suspended nanoparticles in the hybrid nanofluid droplet increases with time, and finally deposit over the substrate to form a nanostructured porous residue surface. Although, many researchers have reported the formation of different residue patterns as a result of nanofluid or hybrid nanofluid droplet evaporation [29–32], there is still a lack of research on how the deposited residue affects the evaporation rate of the subsequent hybrid nanofluid droplet resting on its surface formed by the first evaporating hybrid nanofluid droplet. This phenomenon may be highly relevant to hybrid nanofluid based spray cooling or dropwise cooling applications, where the residue formed by the first evaporating hybrid nanofluid droplet may improve the evaporation rate of the subsequent hybrid nanofluid droplets, and thus may have a higher cooling effect in such applications.

In our previous study [14], we have shown that the deposited residue substantially improves the wetting properties of the copper substrate. This tremendously increases the evaporation rate (~163-196%) of the subsequent hybrid nanofluid droplet resting on the residue surface as compared to the pure copper surface. Also, high surface wettability of the deposited residue improves spreading dynamics of the subsequent hybrid nanofluid droplet, resulting in large liquid-vapor interfacial area and high evaporation rates. Moreover, the suspended nanoparticles increase

98 disjoining pressure near the droplet edge, thus improving droplet spreading over the substrate [33–

99 35]. Droplet spreading, which affects the evaporation rate of subsequent droplet over the residue

100 surface, is divided into three main regimes, the inertial spreading regime (high inertial forces), the

101 capillary spreading regime (high capillary forces) and the gravitational spreading regime

102 (gravitational forces affect spreading) [36].

103

104 This study aims to investigate the evaporation rate of the Ag-GNP hybrid nanofluid droplet on two

105 different types of surfaces, i.e. a pure copper surface and a residue surface formed by the

106 evaporation of first Ag-GNP hybrid nanofluid droplet. It is a well-known fact that nanofluid or

107 hybrid nanofluid droplet leaves behind a residue on the substrate at the end of evaporation [29–

108 32]; however, there is no study to date on how this residue affects the wettability and evaporation

109 rate of the subsequent hybrid nanofluid droplet that sits over the residue surface. The deposited

110 residue may transform the substrate into a highly wetted surface, which may improve the spreading

111 and evaporation rate of the subsequent droplet resting on it. Besides having a synergistic thermal

112 conductivity of the Ag-GNP hybrid nanofluid droplet, which may result in high evaporation rates,

113 its droplet residue also plays a key role, which is to further enhance the evaporation rate of the

114 subsequent Ag-GNP hybrid nanofluid droplet resting on its surface. Therefore, the evaporation

115 rate of the subsequent Ag-GNP hybrid nanofluid droplet is investigated for various residue sizes,

116 resulting from the evaporation of first Ag-GNP hybrid nanofluid droplet. Moreover, this study also

117 highlights the fundamental underlying mechanisms that affect the hybrid nanofluid droplet

118 evaporation rate, such as the wetting characteristics, spreading dynamics and residue surface

119 properties.

120

121 The main novelty of this research is to study the effect of the Ag-GNP hybrid nanofluid mixing

122 ratio on droplet evaporation rate. The droplet wetting characteristics, as well as the residue surface

123 properties, vary considerably with the varying mixing ratio, which eventually affects the droplet

124 evaporation rate. Therefore, the proposed research is focused to determine the Ag-GNP hybrid

125 nanofluid mixing ratio which gives the highest evaporation rate on its respective residue surface.

126 Another novel aspect of proposed research is the manipulation of subsequent hybrid nanofluid

127 droplet wetting characteristics (contact angle and contact diameter), based on the residue size of

128 first evaporated hybrid nanofluid droplet. Droplet wetting manipulation can be important for

129     applications, such as the dropwise hotspot cooling in microelectronics, where the residue size of
130     the first evaporated hybrid nanofluid droplet can be used to manipulate the contact angle and,
131     eventually, the evaporation rate of the subsequent hybrid nanofluid droplet. Based on the above
132     discussion, the main objectives of this research are as follows:

133

134     •   To study the effect of Ag-GNP hybrid nanofluid mixing ratio on droplet evaporation rate;
135     •   To study the effect of residue size, resulting from the evaporation of first hybrid nanofluid
136         droplet, on the evaporation rate of the subsequent hybrid nanofluid droplet;
137     •   To identify the residue surface properties that affect the droplet evaporation rate.

138

139 **2.   Experimental Methodology**

140 In this section, we firstly discuss the experimental techniques that were used in the synthesis of
141 the Ag-GNP hybrid nanofluid. Later, we discuss the methodology that we used to study the droplet
142 evaporation, droplet spreading, and wetting and residue characterization of the Ag-GNP hybrid
143 nanofluid.

144

145     *2.1. Hybrid Nanofluid Synthesis*

146 The Ag-GNP hybrid nanofluid was prepared by a two-step method, in which Ag and GNP
147 nanoparticles were dispersed in water, pre-treated and then ultra-sonicated for two hours [37]. A
148 detailed procedure for synthesis of the Ag-GNP hybrid nanofluid and criteria for selecting this
149 combination (Ag-GNP) in proposed research is discussed in our previous study [14]. Both, GNP
150 (carbon>70% and oxygen>10% by weight, polycarboxylate functionalized) and Ag (particle
151 size<100nm, polyvinylpyrroledone) nanoparticles were purchased from Sigma Aldrich and the
152 prepared Ag-GNP hybrid nanofluid samples were found stable for several hours. The Ag-GNP
153 hybrid  nanofluid was prepared at a fixed particle concentration of 0.1% volume fraction (as the
154 particle concentration effect on the droplet evaporation rate was not the main focus of our research)
155 and various mixing ratios (as shown in Table 1). The droplet evaporation rate and its residue
156 wetting behavior for the Ag-GNP hybrid nanofluid was investigated and compared with Ag and
157 GNP nanofluids, as discussed in the following sub-section 2.2.

## 2.2. Droplet Evaporation, Spreading and Wetting Measurements

In this section, we first discuss the experimental technique that we used to study the Ag-GNP nanofluid/hybrid nanofluid droplet evaporation and wetting characteristics (contact angle and contact diameter) over the residue surface, formed by the evaporation of first Ag-GNP nanofluid/hybrid nanofluid droplet. In the second part, we discuss the same experimental technique but with slightly different settings, to study the spreading behavior of the subsequent Ag-GNP nanofluid/hybrid nanofluid droplets over their respective residue surfaces.

The experimental setup and procedure to measure the droplet evaporation rate and wetting characteristics (such as the contact angle and contact diameter) using an optical tensiometer is explained in detail in our previous study [14]. The main advantage of using an optical tensiometer is that the droplet volume, along with its wetting properties, can be measured at each time step. The temperature inside the test section of tensiometer was kept the same as the room temperature $T$=22 °C, to keep all the three phases (droplet, substrate and air) at thermal equilibrium. Wet air, at an extremely low flow rate (to minimize the advection effects), was introduced into the environmental chamber covering the test section of the tensiometer to maintain the relative humidity fixed at $\varphi$=0.3, in all our experiments. The reason to keep a low relative humidity of $\varphi$=0.3 in our experiments was to reduce the droplet evaporation time, as droplets take more time to evaporate at high humidity values. As the humidity effect on droplet evaporation rate was not the main focus of our research, therefore, it was fixed at $\varphi$=0.3 in all our experiments. The droplet images during the evaporation process were recorded at 14 frames per second. The measurements for Ag-GNP nanofluid/hybrid nanofluid droplet evaporation and wetting properties follow a two-step process as discussed by Siddiqui et al. [14]. We used four different droplet volume ratios ($V_{fd}/V_{sd}$) as 1, 5, 10 and 20 in our experiments, where we fixed the volume of the second droplet as $V_{sd}$=3µl, while only the volume of the first droplet ($V_{fd}$) was increased to allow spreading of the second droplet onto the residue developed by the first droplet. We performed each experiment three times at different locations on the copper surface.

The droplet evaporation and wetting experiments were followed by the experiments on spreading dynamics of the Ag/GNP nanofluid/hybrid nanofluid droplets over their respective residue surfaces, by using the same optical tensiometer technique. The residue samples were prepared by

following the same two-step process [14] as used in the droplet evaporation experiments. However, due to the fast spreading dynamics, which only lasted for a few seconds, the droplets were recorded at a high frame rate of 28 frames per second. The tensiometer video camera recorded the droplet images as it came out of the dispenser until it reached a quasi-equilibrium state (droplet spreading ends macroscopically). The experimental techniques used in residue characterization are discussed in the following sub-section 2.3.

### *2.3. Residue Measurements*

The porous structure of the Ag-GNP nanofluid/hybrid nanofluid droplet residues were characterized by using a scanning electron microscope (TM 3030, Hitachi, Japan). Each measurement was performed three times at different locations on a residue surface, using 3000x magnification. The micrographs were post-processed using an ImageJ software, in order to determine the pore size (Feret diameter) and residue areal porosity, with a maximum mean standard deviation of 0.135 µm and 2.3%, respectively. The roughness parameters (surface roughness ($R_a$) and roughness ratio ($r$)) of droplet residues were measured by using an optical profiler (NPFLEX, Bruker, USA), with a maximum mean standard deviation of 0.26 µm. A 10x objective and a green light for illumination were used during the surface roughness measurements. The surface free energy ($\gamma_{sv}$) of each droplet residue was measured on an optical tensiometer, by using a polar fluid (water) and a dispersive fluid (diiodomethane) based on OWRK/Fowkes model [38], with a maximum mean standard deviation of 1.7mN/m. Also, the droplet surface tension ($\gamma_{lv}$) and its solid-liquid interfacial tension ($\gamma_{sl}$) were measured using an optical tensiometer.

### 3. Theoretical Modelling of Ag-GNP Nanofluid/Hybrid Nanofluid Droplet Evaporation on its Porous Residue Surface

A theoretical model is developed to estimate the instantaneous evaporation rate of the subsequent Ag-GNP nanofluid/hybrid nanofluid droplet over the residue surface developed by the first evaporated Ag-GNP nanofluid/hybrid nanofluid droplet. The schematics of the Ag-GNP nanofluid/hybrid nanofluid droplet over its respective residue surface is shown in Fig. 1(a). The droplet height is denoted as $h_1$, while the height of the vapor equilibrium surface (*VES*) is denoted as $h_2$, as illustrated in Fig. 1(a). The vapor equilibrium surface (*VES*) is the hypothetical surface above the droplet, where the vapor concentration is in equilibrium with the ambient conditions,

220 i.e., $x_{v,2} = \varphi_2 x_{v,1}$ where $\varphi_2 = 0.3$. Moreover, fully saturated vapor conditions ($x_{v,1} = P_{v,sat}/P_a$)

221 are assumed at the droplet-air interface, while the air-vapor mixture above the droplet is assumed

222 as an ideal gas.

223 As both the droplet and the substrate are at room temperature and all the three phases (droplet,

224 substrate and air) are at thermal equilibrium in this study, the proposed evaporation model is based

225 on Fick's Law of mass diffusion and isothermal steady-state assumption. Although wet air (at

226 extremely low flow rate) was induced inside the environmental chamber to control humidity in our

227 experiments, the stationary medium approximation [39] is considered in the proposed model with

228 negligible advection effects. Based on our experimental observation, only droplet height varies,

229 while the contact diameter remains constant (pinning effect) during droplet evaporation. Therefore,

230 one-dimensional diffusion along the height ($h$) is assumed in our model, as shown in Fig. 1 (b).

231 Furthermore, all droplets are assumed as spherical caps (negligible gravitational effect), since the

232 contact radius remains within the capillary length ($l_{ca} = \sqrt{\gamma_{lv}/\rho g}$) during droplet spreading over

233 the residue surface. As the droplet size is larger than the residue surface roughness by 2-3 orders

234 of magnitude in our proposed study, Wenzel approximation [40] holds and the nanofluid/hybrid

235 nanofluid droplet is assumed to completely fill the pores underneath it. The evaporation model is

236 developed based on three input parameters as the droplet height ($h_1$), quasi-equilibrium contact

237 diameter ($\emptyset_{qe}$) and the vapor concentration gradient $dx_v/dh$. The instantaneous droplet

238 evaporation flux $\dot{E}''_{ins}$ ($\mu l/s.m^2$) is determined as [39]:

239

$$\dot{E}''_{ins} = \frac{-MCD}{\rho}\left(\frac{dx_v}{dh}\right), \qquad (1)$$

241

242 and the instantaneous droplet evaporation rate $\dot{E}_{ins}$ ($\mu l/s$) is given as:

243

$$\dot{E}_{ins} = \frac{-MCD}{\rho}\left(\frac{dx_v}{dh}\right)A_s, \qquad (2)$$

245

246 where $M, C, D, \rho$ and $A_s$ are the molar mass of water (g/mol), total molar concentration of air-

247 vapor mixture (mol/m$^3$), mass diffusivity of vapor into the air (m$^2$/s), water density (kg/m$^3$) and

248 the droplet-air interfacial area (m$^2$), respectively. $dx_v/dh$ is the vapor concentration gradient

249 between the droplet-air interface ($x_v = x_{v,1}$) and the vapor equilibrium surface ($x_v = x_{v,2}$), as

9

shown in Fig. 1(a). The total molar concentration of air-vapor mixture ($C$) above the droplet is determined from the ideal gas law as:

$$C = P_a/RT \, , \tag{3}$$

where $P_a$ and $T$ are the ambient pressure and temperature as 101.325 kPa and 22 °C (room temperature), respectively, and $R$ is the universal gas constant ($R$=8.314 J/molK). Since $A_s = \pi\left[(\emptyset_{qe}/2)^2 + h_1{}^2\right]$, equation (2) can be written as:

$$\dot{E}_{ins} = k\left(\frac{dx_v}{dh}\right)\left[(\emptyset_{qe}/2)^2 + h_1{}^2\right] \, , \tag{4}$$

where $k = -\pi MCD/\rho$ is a constant, $\emptyset_{qe}$(m) is the quasi-equilibrium contact diameter (contact diameter at an instant when droplet spreading ends macroscopically) and $h_1$(m) is the droplet height. The unknowns in equation (4) are $\emptyset_{qe}$, $h_1$ and $dx_v/dh$ and, therefore, we need to develop relations for each of these unknowns. We first develop a relation to determine the quasi-equilibrium contact diameter ($\emptyset_{qe}$) for considered nanofluid/hybrid nanofluid droplets. Although we have measured $\emptyset_{qe}$ in our experiments, we further develop a relation based on the Young equation and droplet geometry, and subsequently compare the theoretical and measured values of $\emptyset_{qe}$ (see Fig. 4(c)). The droplets studied in proposed research exhibit different quasi-equilibrium contact diameters, due to their different surface tensions as well as varying surface chemistry, and surface roughness of their corresponding residues. The Young equation is given as [41]:

$$\theta_y = cos^{-1}\left(\frac{\gamma_{sv}-\gamma_{sl}}{\gamma_{lv}}\right) \quad , \tag{5}$$

where $\theta_y$ is the Young contact angle and $\gamma_{sv}$, $\gamma_{sl}$ and $\gamma_{lv}$ are the interfacial tensions at the three-phase contact line of a sessile droplet. Based on the Wenzel effect [42], we get:

$$\theta_{qe} = cos^{-1}\left(rcos\theta_y\right) , \tag{6}$$

where $r$ is the roughness ratio and $\theta_{qe}$ is the contact angle at a quasi-equilibrium state. The measured values for $r$, $\theta_a$ and interfacial tensions ($\gamma_{sv}$, $\gamma_{sl}$ and $\gamma_{lv}$) for Ag-GNP nanofluid/hybrid nanofluid droplets and their respective residue surfaces are given in Table 1. It should be noted that $\theta_{qe}$ is the theoretical contact angle, while $\theta_a$ is the measured or apparent contact angle at a quasi-equilibrium state. The quasi-equilibrium contact angle ($\theta_{qe}$) from equation (6) is used to determine the quasi-equilibrium contact diameter ($\emptyset_{qe}$), as given by the following spherical-cap equation:

$$\emptyset_{qe} = \left( \frac{24 V_{as} \sin\theta_{qe}(1+\cos\theta_{qe})}{\pi(2+\cos\theta_{qe})(1-\cos\theta_{qe})} \right)^{1/3} . \tag{7}$$

where $V_{as}$ is the droplet volume above the residue surface. It should be noted that equation (7) is only applicable for unbounded residue surfaces, where the droplet spreading is not restricted by the residue boundaries. For cases, where the droplet contact diameter is the same as the residue diameter (completely wetted residue), $\emptyset_{qe}$ is considered equal to the residue diameter. As the droplet spreads over the residue surface, it fills the pores underneath it and, therefore, the net droplet volume ($V_{net}$=3µl) is equal to the sum of the droplet volume above the residue surface ($V_{as}$) and the droplet volume below the residue surface ($V_{bs}$). The droplet volume above the residue surface is given as:

$$V_{as} = V_{net} - V_{bs} \quad , \tag{8}$$

The droplet volume below the residue surface is determined as:

$$V_{bs} = \pi a_p R_a (\emptyset_{qe}/2)^2 . \tag{9}$$

where $a_p$ and $R_a$ are the areal porosity and average surface roughness of the droplet residue respectively, and their measured experimental data is shown in Table 2. Since the variation in droplet volume above the residue surface ($V_{as}$) occurs due to evaporation, as well as the droplet entrainment into the residue pores during the droplet spreading process, the droplet evaporation rate is determined in the interval when the droplet reaches a quasi-equilibrium state (droplet

11

spreading ends at macroscopic scale), until the end of the evaporation process. Another unknown term in the equation (4) is the droplet height ($h_1$), which is determined from the spherical-cap geometry as:

$$h_1 = \sqrt{\frac{\emptyset_{qe}^2}{2(1+cos\theta_s)} - \frac{\emptyset_{qe}^2}{4}} \quad .$$ (10)

where $\theta_s$ is the static contact angle and this varies with time during the droplet evaporation process (see Fig. 5). We have determined relations for two unknown terms ($\emptyset_{qe}, h_1$) of equation (4) and now we determine a relation for term $dx_v/dh$. An empirical model is developed to estimate the term $dx_v/dh$, as a function of the static contact angle, mixing ratio and $V_{fd}/V_{sd}$, by using our experimental data. The non-dimensional form of this equation is given as:

$$\frac{A}{h_c}\frac{dx_v}{d\tilde{h}} = Bf\left(\theta_s, MR, \frac{V_{fd}}{V_{sd}}\right) ,$$ (11)

where $A$ and $B$ are the equation coefficients and $h_c$ is the characteristic height equal to $A/B$. As both $A$ and $B$ are equal to unity, $h_c$ =1mm. Thus, $\emptyset_{qe}$, $h_1$ and $dx_v/dh$ from equations (7), (10) and (11) are used in equation (4) respectively, to determine the instantaneous evaporation rate of all studied droplets. It must also be noted, that in equation (4), both $\emptyset_{qe}$ and $h_1$ are the theoretical values, while $dx_v/dh$ is obtained from the empirical model as discussed in the supplementary material. The height ($h_2$) of the vapor equilibrium surface (*VES*) can be determined from Equation (11) as:

$$x_{v,2} - x_{v,1} = f\left(\theta_s, MR, \frac{V_{fd}}{V_{sd}}\right) h_c(\tilde{h}_2 - \tilde{h}_1) \quad ,$$ (12)

$$h_2 = \tilde{h}_2 h_c = \left(\frac{x_{v,2}-x_{v,1}}{f\left(\theta_s, MR, \frac{V_{fd}}{V_{sd}}\right)}\right) + h_1 \quad .$$ (13)

## 4. Results and Discussion

This section is divided into three main parts. In the first part, the evaporation rate of all considered nanofluid and hybrid nanofluid droplets for various droplet volume ratios ($V_{fd}/V_{sd}$) is discussed. The second part includes discussion on main factors that affect the droplet evaporation rate, such as the wetting behavior of the nanofluid/hybrid nanofluid droplets on their respective residue surfaces. The droplet spreading dynamics over the residue surface is considered, followed by the discussion on wetting behavior, at both the quasi-equilibrium state and during the droplet evaporation process. The last part is focused on the residue characterization, in which the surface chemistry, porosity and roughness parameters are analyzed, in order to understand how these parameters affect the droplet evaporation rate.

### 4.1. Droplet Evaporation Rate

The net evaporation rate of the Ag/GNP nanofluid and hybrid nanofluid droplets on various substrates is illustrated in Fig. 2(a). The results show that the droplet evaporation rate is almost the same for all mixing ratios when copper is used as a substrate. However, the net evaporation rate varies remarkably, depending on the hybrid nanofluid mixing ratio and the droplet residue size (i.e., $V_{fd}/V_{sd}$). It is observed that the net evaporation rate is increased by about 4 times, as $V_{fd}/V_{sd}$ is increased from 1 to 20 in GNP nanofluid and MR-1 hybrid nanofluid droplets. However, the effect of $V_{fd}/V_{sd}$ on evaporation rate starts diminishing, moving from MR-2 to MR-5 hybrid nanofluid droplets, until we reach the Ag nanofluid droplet. For the Ag nanofluid droplet, the residue size has an inverse effect on the droplet evaporation rate. That is, the evaporation rate decreases with an increasing value of $V_{fd}/V_{sd}$. The main reason for anomalous evaporation rate of the Ag nanofluid droplet is the increase in surface roughness with increasing residue size, which consequently increases the non-wetting characteristics of the residue surface (Wenzel effect [42]), as further discussed in sub-section 4.2. It is also shown in Fig. 2(a) that the evaporation rate is considerably increased for GNP nanofluid and MR-1 to MR-3 hybrid nanofluid droplets, residing on their respective residue surfaces (for $V_{fd}/V_{sd} \geq 5$), as compared to that on the copper surface.

Fig. 2(b) shows a linear relationship between the net droplet evaporation rate and the quasi-equilibrium interfacial surface area, for all considered nanofluid/hybrid nanofluid droplets. Furthermore, the net droplet evaporation rate decays as a power law function of the quasi-

366 <mark>equilibrium contact angle, as shown by the inset in Fig. 2(b). This shows that large quasi-</mark>

367 <mark>equilibrium contact angle and small quasi-equilibrium interfacial surface area leads to low droplet</mark>

368 <mark>evaporation rate.</mark> The variation in droplet height ($h_1$) and *VES* height ($h_2$) with the residue size

369 ($V_{fd}/V_{sd}$) of the Ag-GNP nanofluid/hybrid nanofluid droplets, at a quasi-equilibrium state is shown

370 in Fig. 2(c). It is noticed that the droplet height ($h_1$) is considerably reduced (by about 4 times), as

371 $V_{fd}/V_{sd}$ is increased from 1 to 20 for GNP nanofluid and MR-1 hybrid nanofluid droplets. The *VES*

372 is also shifted downwards with decreasing droplet height ($h_1$), however, the difference between $h_1$

373 and $h_2$ grows substantially with increasing values of $V_{fd}/V_{sd}$. This is because the *VES* height ($h_2$) is

374 not considerably affected by the variation in the droplet height ($h_1$). Moreover, $V_{fd}/V_{sd}$ has a

375 reduced effect on the droplet height ($h_1$) and the *VES* height ($h_2$), as we move from MR-2 to MR-

376 5 hybrid nanofluid. Conversely, for the Ag nanofluid, the droplet height ($h_1$) increases as $V_{fd}/V_{sd}$ is

377 increased, which consequently increases the *VES* height ($h_2$). The main reasons for varying droplet

378 height ($h_1$), with increasing values of $V_{fd}/V_{sd}$, are discussed in the next sub-section 4.2.

379

380 The variation in volume with time during the course of Ag-GNP nanofluid/hybrid nanofluid

381 droplet evaporation is presented in Fig. 3. The volume is normalized with respect to the initial

382 droplet volume ($V_i$) at a quasi-equilibrium state, while the time is normalized with respect to the

383 total evaporating time ($t_f$) for each droplet on the Cu surface. The main reason for normalizing time

384 with respect to the Cu surface is to compare the total droplet evaporation time on each residue

385 surface with that on the Cu surface. It is noticed that the total evaporation time on Cu surface and

386 residue surface with $V_{fd}/V_{sd}$=1 is almost the same for all studied nanofluid/hybrid nanofluid

387 droplets. However, the evaporation time is significantly reduced, as $V_{fd}/V_{sd}$ is increased from 5 to

388 20 for GNP nanofluid and MR-1 hybrid nanofluid droplets. Furthermore, $V_{fd}/V_{sd}$ has a reduced

389 effect on the total evaporation time, moving from MR-2 to MR-5 hybrid nanofluid droplets.

390 Conversely, the evaporation time of the Ag nanofluid droplet on its residue surface is higher than

391 that on the Cu surface. It is noticed that the theoretical results obtained from equation (4) agree

392 well with the experimental data, as illustrated in Fig. 3. The main factors responsible for different

393 evaporation rates of Ag-GNP nanofluid/hybrid nanofluid droplets are discussed in the following

394 sub-section 4.2.

395

### 4.2. Spreading Dynamics and Wetting Characteristics

The spreading dynamics and wetting behavior of the studied nanofluid/hybrid nanofluid droplets, over their respective residue surfaces, play a key role in the net droplet evaporation rate. This is because the evaporation rate depends on the droplet-air interfacial area, which in turn depends on the droplet spreading and wetting behavior over the residue surfaces. This section is divided into three main parts. In the first part, the spreading dynamics of the nanofluid/hybrid nanofluid droplets over their respective residue surfaces is discussed. The second part is focused on wetting behavior at a quasi-equilibrium state, when the droplet spreading ends at the macroscopic scale. In the last part, the variation in the static contact angle and contact diameter, induced by the droplet evaporation, is discussed for all considered droplets.

Fig. 4(a) and (b) shows the spreading dynamics of Ag-GNP nanofluid/hybrid nanofluid droplets over their respective residue surfaces at $V_{fd}/V_{sd}$=20. It must be noted that the spreading nanofluid/hybrid nanofluid droplets do not reach their residue boundaries at $V_{fd}/V_{sd}$=20. Therefore, the droplet spreading remains unbounded, and is only affected by the residue surface properties and interfacial tensions at the three-phase contact line. It is noticed that all droplets initially undergo a very high spreading rate in the inertial regime (first few points in Fig. 4(a) and (b)), which is followed by the capillary regime, in which the capillary forces overcome inertial forces, until we reach a quasi-equilibrium state. As shown in Fig. 4(a) and (b), GNP nanofluid and MR-1 hybrid nanofluid droplets show significant spreading, due to highly wetted surfaces, resulting from high roughness ($r$) and surface free energy of their respective residues (Table 1). Such a rapid spreading over highly wetted residue surfaces results in a large droplet-air interfacial area, which substantially improves the droplet evaporation rate. Despite having relatively low surface tension for MR-2 to MR-5 hybrid nanofluid droplets (Table 1), the droplet spreading is reduced, due to the low surface roughness and surface free energy of their residues. On the other hand, the Ag nanofluid droplet spreads inwardly in the inertial regime (as shown in the inset of Fig. 4(a)) due to its non-wetted residue, and quickly attains a quasi-equilibrium state, as compared to other droplets. As the spreading is in the outward direction for GNP nanofluid and MR-1 to MR-5 hybrid nanofluid droplets, a semi-empirical asymptotic relation is developed, to estimate the dynamic contact diameter ($\emptyset_{d}$) as a function of spreading time ($t$), and given as:

427
$$\emptyset_d = \emptyset_{qe} \left(1 - e^{-\frac{t}{\tau}}\right)^n \ , \tag{14}$$

428

429 where $\tau$ is the droplet spreading time scale to reach a quasi-equilibrium state and includes both the

430 initial inertial spreading and the subsequent capillary spreading regimes and given as:

431

432
$$\tau = \frac{\pi^7 \mu V_{as}^{4/3}}{\gamma_{lv} R_a \emptyset_{qe}^2} \ . \tag{15}$$

433

434 For the Ag nanofluid droplet, spreading is in the inward direction, due to a highly non-wetted

435 residue surface, and the dynamic contact diameter ($\emptyset_{d,Ag}$) is estimated by the following semi-

436 empirical relation:

437

438
$$\emptyset_{d,Ag} = \emptyset_{qe} \left(1 + e^{-\frac{t}{\tau}}\right)^n , \tag{16}$$

439
440 where,
441

442
$$\tau_{Ag} = \frac{\mu V_{as}^{4/3}}{\gamma_{lv} R_a \emptyset_{qe}^2} \ . \tag{17}$$

443

444 where $n$ is equal to 0.1, 0.033, 0.034, 0.011, 0.133, 0.055 and 0.042 for GNP nanofluid, MR-1

445 hybrid nanofluid, MR-2 hybrid nanofluid, MR-3 hybrid nanofluid, MR-4 hybrid nanofluid, MR-5

446 hybrid nanofluid and Ag nanofluid droplets. The semi-empirical equations (15) and (17),

447 pertaining to the droplet spreading time scale, were developed using the experimental data. It is

448 noticed in Fig. 4(a) that the droplet spreading time scale ($\tau$) is increased, as we move from GNP

449 nanofluid to MR-5 hybrid nanofluid, followed by a very low value of $\tau$ for Ag nanofluid. Such a

450 low value of droplet spreading time scale for the Ag nanofluid droplet is also evident from the

451 experimental data shown in Fig. 4(a), in which the droplet after a short inertial regime (shown in

452 the inset) quickly gains a quasi-equilibrium state. The dynamic contact angle ($\theta_d$) of spreading

453 droplets, at any instantaneous time (*t*), is determined by solving an implicit equation for a

454 spherical-cap, with known values of $V_{as}$ (equation (8)) and $\emptyset_d$ (equations (14) and (16)), and given

455 as:

456

$$3V_{as}sin\theta_d(cos\theta_d + 1) + \frac{\pi\emptyset_d{}^3}{4}(cos\theta_d - 1)\left(1 + \frac{cos\theta_d}{2}\right) = 0 \ . \tag{18}$$

It is noted that the semi-empirical results from equations (14) and (16) as well as theoretical results from equation (18) agree well with the experimental data, as shown in Fig. 4(a) and (b). Since the droplet evaporation rate depends on the spreading behavior, these relations can be used to predict the spreading dynamics of the Ag-GNP nanofluid/hybrid nanofluid droplets over their respective residue surfaces. Fig. 4(c) shows the quasi-equilibrium contact angle ($\theta_{qe}$) and the quasi-equilibrium contact diameter ($\emptyset_{qe}$) for all considered nanofluid/hybrid nanofluid droplets at $V_{fd}/V_{sd}$=20. The insets of Fig. 4(c) illustrate the droplet images at a quasi-equilibrium state. It is observed that both GNP nanofluid and MR-1 hybrid nanofluid droplets show promising wetting characteristics (low contact angle and large contact diameter) on their highly wetted residue surfaces, which results in large evaporation rates. However, the wetting properties are adversely affected (high contact angle and small contact diameter), moving from MR-2 to MR-5 hybrid nanofluid droplets, while poor wetting is observed for the Ag nanofluid droplet on its highly non-wetted residue surface, which results in low evaporation rates. The quasi-equilibrium contact angle and contact diameter for all considered droplets at $V_{fd}/V_{sd}$=20 are correlated by an exponential function, as shown in Fig. 4(c). Also, the contact angle and contact diameter obtained from equations (6) and (7) at a quasi-equilibrium state show a good agreement with the experimental data.

Fig. 4(d) shows the effect of the droplet residue size ($V_{fd}/V_{sd}$) on the quasi-equilibrium contact angle ($\theta_{qe}$) of the Ag-GNP nanofluid/hybrid nanofluid droplets. It is observed that the GNP nanofluid and MR-1 hybrid nanofluid droplets completely wet their respective residues, with $\theta_{qe} \approx 100°$, $\theta_{qe} \approx 41°$, $\theta_{qe} \approx 22°$ for $V_{fd}/V_{sd}$=1, $V_{fd}/V_{sd}$=5 and $V_{fd}/V_{sd}$=10, respectively. However, the residue at $V_{fd}/V_{sd}$=20 remains partially wetted, despite having a highly wetted surface ($\theta_{qe} \approx 10°$). It is also noteworthy that the droplets do not spread beyond the residue boundaries, for $V_{fd}/V_{sd}$=1 to $V_{fd}/V_{sd}$=10, due to the low surface free energy of the Cu surface ($\gamma_{sv}$ =33 mN/m). This suggests that the droplet wetting characteristics (contact angle and contact diameter) can be manipulated by its residue size, for cases where the droplets reach up to the residue boundaries. Increasing residue size increases droplet spreading on a highly wetted residue surface for GNP nanofluid and MR-1 hybrid nanofluid droplets. This increases the interfacial surface area and the

17

droplet evaporation rate. Moreover, MR-2 and MR-3 hybrid nanofluid droplets completely wet their residues for $V_{fd}/V_{sd}$=1 ($\theta_{qe} \approx 100°$) and $V_{fd}/V_{sd}$=5 ($\theta_{qe} \approx 41°$), while partial wetting is observed for $V_{fd}/V_{sd}$=10 ($\theta_{qe} \approx 26°$) and $V_{fd}/V_{sd}$=20 ($\theta_{qe} \approx 24°$). MR-4 and MR-5 hybrid nanofluids and Ag nanofluid only show complete wetting for $V_{fd}/V_{sd}$=1 ($\theta_{qe} \approx 100°$), while their residues remain partially wetted for $V_{fd}/V_{sd}$=5, $V_{fd}/V_{sd}$=10 and $V_{fd}/V_{sd}$=20. Furthermore, unlike other nanofluid/hybrid nanofluid droplets, the quasi-equilibrium contact angle for the Ag nanofluid droplet increases with increasing values of $V_{fd}/V_{sd}$. This is because of the increase in surface roughness with residue size (as shown in Table 2), which makes the surface increasingly non-wetted, as the residue size is increased.

Fig. 5 shows the variation in contact angle and contact diameter, due to the Ag-GNP nanofluid/hybrid nanofluid droplet evaporation on the Cu surface, and their respective residue surfaces, for different values of $V_{fd}/V_{sd}$. It is noticed that the droplet remains pinned for most part of the droplet evaporation (constant contact diameter), while some depinning is observed near the end of the droplet evaporation, for all considered nanofluid/hybrid nanofluid droplets. The main reason for the pinning effect in the studied droplets is the migration of nanoparticles/hybrid nanoparticles near the three-phase contact line of the evaporating droplet. On the other hand, the contact angle varies with time during the course of the nanofluid/hybrid nanofluid droplet evaporation. It is observed that the contact angle reduction rate is almost the same for all studied droplets, when Cu and residue with $V_{fd}/V_{sd}$=1 are used as substrates. As both Cu and residue with $V_{fd}/V_{sd}$=1 show poor wettability ($\theta_{qe} \approx 100° - 140°$) for all studied droplets, this results in small liquid-vapor droplet interfacial areas and subsequently low evaporation rates. Moreover, the contact angle reduction rate is non-uniform for these cases. On the other hand, the contact angle reduction rate is nearly constant for all nanofluid/hybrid nanofluid droplets (except the Ag nanofluid droplet), when $V_{fd}/V_{sd} \geq 5$. For the Ag nanofluid droplet, evaporation occurs at non-uniform contact angle reduction rates for all $V_{fd}/V_{sd}$ values, due to a highly non-wetted residue surface. In order to understand the underlying mechanisms for wetting transition, from a highly wetted GNP nanofluid/MR-1 hybrid nanofluid droplet residue surface ($\theta_{qe} \approx 10°$) to a highly non-wetted Ag nanofluid droplet residue surface ($\theta_{qe} \approx 142°$), all droplet residues are characterized, as discussed in the next sub-section 4.3.

18

### 4.3. Droplet Residue Surface Characteristics

The residue surface properties such as the porosity and surface roughness directly affect the droplet evaporation rate. A porous surface with high surface roughness leads to high droplet spreading on its surface and it increases the liquid-air interfacial area and the droplet evaporation rate. The measured data on residue surface properties is shown in Table 2. It is noticed that the mean Feret Diameter (pore size), areal porosity and surface roughness decrease, as we proceed from GNP nanofluid/MR-1 hybrid nanofluid to MR-5 hybrid nanofluid/Ag nanofluid droplet residues. Conversely, the mean Feret Diameter, areal porosity and surface roughness increase with increasing residue size, for each nanofluid/hybrid nanofluid droplet residue. A similar trend is observed for variation in droplet evaporation rate with respect to the mixing ratio and the residue size. This suggests that the evaporation rate of subsequent droplet is affected by the residue surface properties. It must also be noted that the droplet volume ($V_{fd}$) in Table 2 refers to the volume of the first nanofluid/hybrid nanofluid droplet, which we used to develop the residue on the Cu surface. More details on residue surface properties, such as the residue surface morphology and pore size distribution, can be obtained from supplementary material.

The droplet evaporation rate also depends on the residue surface free energy. The surface free energy of the Cu surface, as well as the Ag-GNP nanofluid/hybrid nanofluid droplet residue surfaces, is shown in Fig. 6. It is observed that the surface free energy decreases, as we move from the GNP nanofluid droplet residue to the Ag nanofluid droplet residue. The surface free energy of each residue is compared with the uncorrected (includes roughness effects) surface free energy, as shown in Fig. 6. It is noticed that the GNP nanofluid and MR-1 hybrid nanofluid droplet residues give the highest uncorrected surface free energy, with large polar components, which results in highly wetted surfaces, and eventually give high evaporation rates for respective droplets residing on these surfaces. However, the surface free energy, as well as its polar component, decrease, as we move from MR-2 to MR-5 hybrid nanofluid droplet residue, and this results in partially wetted surfaces and consequently gives low droplet evaporation rates. The copper surface, and the Ag nanofluid droplet residue surface, both show very low surface free energy values, with negligible polar components, which results in non-wetted surfaces, and gives extremely low evaporation rates for droplets residing on these surfaces.

## 5. Conclusions

Although droplet evaporation offers high heat transfer rates due to a phase change process, such techniques are still not effective for thermal management of high heat flux devices due to the limiting heat removal capacity of conventional fluids, such as water. To address this issue, we have investigated the droplet evaporation of the Ag-GNP hybrid nanofluid, due to its synergistic thermal properties, for various mixing ratios and residue sizes. As a main novelty of our work, we have shown that the evaporation rate of the subsequent Ag-GNP hybrid nanofluid droplet, resting on its residue surface, varies significantly with varying mixing ratio and residue size. Another novelty lies in a range of wetting behavior, from highly wetted GNP nanofluid and MR-1 hybrid nanofluid droplet residues to an extremely non-wetted Ag nanofluid droplet residue, while having partially wetted MR-2 to MR-5 hybrid nanofluid droplet residues. We also showed that large spreading of GNP nanofluid and MR-1 hybrid nanofluid droplets over their respective wetted residues increases the droplet-air interfacial area and it increases the droplet evaporation rate. Moreover, all residues have a porous structure with varying pore size and areal porosity. Also, the residue surface roughness increases with increasing porosity, which leads to increasing wettability and evaporation rate of the subsequent droplets resting on such residue surfaces. Following are the main conclusions of this study:

- MR-1 hybrid nanofluid droplet gives the highest evaporation rate (370% higher than that of the Ag nanofluid droplet) due to a highly wetted residue surface for $V_{fd}/V_{sd}=20$.

- The evaporation rate is remarkably increased by about 285% as $V_{fd}/V_{sd}$ is increased from 1 to 20 for GNP nanofluid and MR-1 hybrid nanofluid droplets resting on their respective residue surfaces.

- The evaporation rate substantially drops moving from MR-2 to MR-5 hybrid nanofluid droplets, while Ag nanofluid droplets give the least evaporation rates for $V_{fd}/V_{sd}\geq5$.

- High droplet spreading is achieved in GNP nanofluid and MR-1 hybrid nanofluid droplets, while the droplet spreading is reduced when moving from MR-2 to MR-5 hybrid nanofluid droplets on their respective residue surfaces.

- The quasi-equilibrium contact angle increases from about 10° in GNP nanofluid and MR-1 hybrid nanofluid droplets to about 142° in Ag nanofluid droplets on their respective residue surfaces.

- The quasi-equilibrium contact angle is reduced from 100° to 10° for GNP nanofluid and MR-1 hybrid nanofluid droplets as $V_{fd}/V_{sd}$ is increased from 1 to 20.
- The pore size (<mark>Feret diameter</mark>) and areal porosity increase with increasing residue size, while they decrease with increasing mixing ratios (MR-1 to MR-5) of hybrid nanofluid droplet residues.

**References**

[1]    M.A. Ebadian, C.X. Lin, A Review of High-Heat-Flux Heat Removal Technologies, J. Heat Transfer. 133 (2011). https://doi.org/10.1115/1.4004340.

[2]    C.Y. Tso, S.C. Fu, C.Y.H. Chao, A semi-analytical model for the thermal conductivity of nanofluids and determination of the nanolayer thickness, Int. J. Heat Mass Transf. 70 (2014) 202–214. https://doi.org/https://doi.org/10.1016/j.ijheatmasstransfer.2013.10.077.

[3]    S. Fu, C. Tso, Y. Fong, C.Y.H. Chao, Evaporation of Al2O3-water nanofluids in an externally micro-grooved evaporator, Sci. Technol. Built Environ. 23 (2017) 345–354. https://doi.org/10.1080/23744731.2016.1250562.

[4]    C.Y. Tso, C.Y.H. Chao, Study of enthalpy of evaporation, saturated vapor pressure and evaporation rate of aqueous nanofluids, Int. J. Heat Mass Transf. 84 (2015) 931–941. https://doi.org/10.1016/j.ijheatmasstransfer.2015.01.090.

[5]    F.R. Siddiqui, C.Y. Tso, K.C. Chan, S.C. Fu, C.Y.H. Chao, On trade-off for dispersion stability and thermal transport of Cu-Al2O3 hybrid nanofluid for various mixing ratios, Int. J. Heat Mass Transf. 132 (2019) 1200–1216. https://doi.org/https://doi.org/10.1016/j.ijheatmasstransfer.2018.12.094.

[6]    G.M. Moldoveanu, G. Huminic, A.A. Minea, A. Huminic, Experimental study on thermal

610     conductivity of stabilized Al2O3 and SiO2 nanofluids and their hybrid, Int. J. Heat Mass

611     Transf.                    127                    (2018)                    450–457.

612     https://doi.org/https://doi.org/10.1016/j.ijheatmasstransfer.2018.07.024.

613     [7]    S. Suresh, K.P. Venkitaraj, P. Selvakumar, M. Chandrasekar, Synthesis of Al2O3–Cu/water

614            hybrid nanofluids using two step method and its thermo physical properties, Colloids

615            Surfaces    A    Physicochem.    Eng.    Asp.    388    (2011)    41–48.

616            https://doi.org/https://doi.org/10.1016/j.colsurfa.2011.08.005.

617     [8]    M.J. Nine, M. Batmunkh, J.-H. Kim, H.-S. Chung, H.-M. Jeong, Investigation of Al2O3-

618            MWCNTs Hybrid Dispersion in Water and Their Thermal Characterization, J. Nanosci.

619            Nanotechnol. 12 (2012) 4553–4559. https://doi.org/10.1166/jnn.2012.6193.

620     [9]    M. Batmunkh, M.R. Tanshen, M.J. Nine, M. Myekhlai, H. Choi, H. Chung, Thermal

621            Conductivity of TiO2 Nanoparticles Based Aqueous Nanofluids with an Addition of a

622            Modified    Silver    Particle,    Ind.    Eng.    Chem.    Res.    53    (2014)    8445–8451.

623            https://doi.org/10.1021/ie403712f.

624     [10]   M.R. Han, Z. H, Yang, B., Kim, S. H., Zachariah, Application of hybrid

625            sphere/carbonnanotube particles in nanofluids, Nanotechnology. 18 (2007) 105–109.

626     [11]   M. Radiom, C. Yang, W.K. Chan, Dynamic contact angle of water-based titanium oxide

627            nanofluid, Nanoscale Res. Lett. 8 (2013) 282. https://doi.org/10.1186/1556-276X-8-282.

628     [12]   D. Chakraborty, G.S. Sudha, S. Chakraborty, S. DasGupta, Effect of submicron particles on

629            electrowetting on dielectrics (EWOD) of sessile droplets, J. Colloid Interface Sci. 363

630            (2011) 640–645. https://doi.org/https://doi.org/10.1016/j.jcis.2011.07.077.

631     [13]   S.J. Hong, T.H. Chou, Y.Y. Liu, Y.J. Sheng, H.K. Tsao, Advancing and receding wetting

632            behavior of a droplet on a narrow rectangular plane, Colloid Polym. Sci. 291 (2013) 347–

633            353. https://doi.org/10.1007/s00396-012-2797-5.

634     [14]   F.R. Siddiqui, C.Y. Tso, S.C. Fu, C.Y.H. Chao, H.H. Qiu, Experimental Investigation On

635            Silver-Graphene Hybrid Nanofluid Droplet Evaporation And Wetting Characteristics Of Its

636            Nanostructured Droplet Residue, in: ASME-JSME-KSME 2019 8th Jt. Fluids Eng. Conf.,

637            San Francisco, 2019: pp. 1–8. https://doi.org/https://doi.org/10.1115/AJKFluids2019-5049.

638    [15]    T.A.H. Nguyen, A. V Nguyen, Increased Evaporation Kinetics of Sessile Droplets by Using
639            Nanoparticles, Langmuir. 28 (2012) 16725–16728. https://doi.org/10.1021/la303293w.

640    [16]    R.D. Deegan, O. Bakajin, T.F. Dupont, G. Huber, S.R. Nagel, T.A. Witten, Contact line
641            deposits in an evaporating drop, 62 (2000) 756–765.

642    [17]    R.D. Deegan, Pattern formation in drying drops, Phys. Rev. E - Stat. Physics, Plasmas,
643            Fluids,        Relat.        Interdiscip.        Top.        61        (2000)        475–485.
644            https://doi.org/10.1103/PhysRevE.61.475.

645    [18]    F.-C. Wang, H.-A. Wu, Pinning and depinning mechanism of the contact line during
646            evaporation of nano-droplets sessile on textured surfaces, Soft Matter. 9 (2013) 5703–5709.
647            https://doi.org/10.1039/C3SM50530H.

648    [19]    R. V Craster, O.K. Matar, K. Sefiane, Pinning, Retraction, and Terracing of Evaporating
649            Droplets      Containing      Nanoparticles,      Langmuir.      25      (2009)      3601–3609.
650            https://doi.org/10.1021/la8037704.

651    [20]    C. Zhang, X. Zhu, L. Zhou, Morphology tunable pinning force and evaporation modes of
652            water droplets on PDMS spherical cap micron-arrays, Chem. Phys. Lett. 508 (2011) 134–
653            138. https://doi.org/https://doi.org/10.1016/j.cplett.2011.04.041.

654    [21]    X. Zhong, A. Crivoi, F. Duan, Sessile nanofluid droplet drying, Adv. Colloid Interface Sci.
655            217 (2015) 13–30. https://doi.org/10.1016/j.cis.2014.12.003.

656    [22]    R.D. Deegan, O. Bakajin, T.F. Dupont, G. Huber, S.R. Nagel, T.A. Witten, Capillary flow
657            as the cause of ring stains from dried liquid drops, Nature. 389 (1997) 827–829.
658            https://doi.org/10.1038/39827.

659    [23]    K. Sefiane, R. Bennacer, Nanofluids droplets evaporation kinetics and wetting dynamics on
660            rough      heated      substrates,      Adv.      Colloid      Interface      Sci.      147–148 (2009)      263–271.
661            https://doi.org/https://doi.org/10.1016/j.cis.2008.09.011.

662    [24]    M. Moghiman, B. Aslani, Influence of nanoparticles on reducing and enhancing evaporation
663            mass transfer and its efficiency, Int. J. Heat Mass Transf. 61 (2013) 114–118.
664            https://doi.org/https://doi.org/10.1016/j.ijheatmasstransfer.2013.01.057.

665      [25]    R.-H. Chen, T.X. Phuoc, D. Martello, Effects of nanoparticles on nanofluid droplet
666             evaporation, Int. J. Heat Mass Transf. 53 (2010) 3677–3682.
667             https://doi.org/https://doi.org/10.1016/j.ijheatmasstransfer.2010.04.006.

668      [26]    H. Hu, R.G. Larson, Evaporation of a Sessile Droplet on a Substrate, J. Phys. Chem. B. 106
669             (2002) 1334–1344. https://doi.org/10.1021/jp0118322.

670      [27]    R.G. Picknett, R. Bexon, The Evaporation of Sessile or Pendant Drops in Still Air, J. Colloid
671             Interface Sci. 61 (1977) 336–350.

672      [28]    Y.O. Popov, Evaporative deposition patterns : Spatial dimensions of the deposit, Phys. Rev.
673             E. 71 (2005) 1–17. https://doi.org/10.1103/PhysRevE.71.036313.

674      [29]    H.H. Lee, S.C. Fu, C.Y. Tso, C.Y.H. Chao, Study of residue patterns of aqueous nanofluid
675             droplets with different particle sizes and concentrations on different substrates, Int. J. Heat
676             Mass Transf. 105 (2017) 230–236.
677             https://doi.org/https://doi.org/10.1016/j.ijheatmasstransfer.2016.09.093.

678      [30]    P.J. Yunker, T. Still, M.A. Lohr, A.G. Yodh, Suppression of the coffee-ring effect by shape-
679             dependent capillary interactions, Nature. 476 (2011) 308–311.
680             https://doi.org/10.1038/nature10344.

681      [31]    T.P. Bigioni, X.-M. Lin, T.T. Nguyen, E.I. Corwin, T.A. Witten, H.M. Jaeger, Kinetically
682             driven self assembly of highly ordered nanoparticle monolayers, Nat. Mater. 5 (2006) 265–
683             270. https://doi.org/10.1038/nmat1611.

684      [32]    M. Amjad, Y. Yang, G. Raza, H. Gao, J. Zhang, L. Zhou, X. Du, D. Wen, Deposition pattern
685             and tracer particle motion of evaporating multi-component sessile droplets, J. Colloid
686             Interface Sci. 506 (2017) 83–92. https://doi.org/https://doi.org/10.1016/j.jcis.2017.07.025.

687      [33]    A. Nikolov, K. Kondiparty, D. Wasan, Nanoparticle Self-Structuring in a Nanofluid Film
688             Spreading on a Solid Surface, Langmuir. 26 (2010) 7665–7670.
689             https://doi.org/10.1021/la100928t.

690      [34]    K. Kondiparty, A.D. Nikolov, D. Wasan, K.-L. Liu, Dynamic Spreading of Nanofluids on
691             Solids. Part I: Experimental, Langmuir. 28 (2012) 14618–14623.
692             https://doi.org/10.1021/la3027013.

693    [35]  D.T. Wasan, A.D. Nikolov, Spreading of nanofluids on solids, Nature. 423 (2003) 156–159.
694           https://doi.org/10.1038/nature01591.

695    [36]  V.M. Starov, M.G. Velarde, C.J. Radke, Wetting and Spreading Dynamics, Taylor and
696           Francis, 2007.

697    [37]  F.R. Siddiqui, C.Y. Tso, K.C. Chan, S.C. Fu, C.Y.H. Chao, Dataset on critical parameters
698           of dispersion stability of $Cu/Al_2O_3$ nanofluid and hybrid nanofluid for various ultra-
699           sonication times, Data Br. 22 (2019) 863–865.

700    [38]  F.M. Fowkes, Attractive forces at interfaces, Ind. Eng. Chem. 56 (1964) 40–52.
701           https://doi.org/10.1021/ie50660a008.

702    [39]  F.P. Incropera, D.P. DeWitt, T.L. Bergman, A.S. Lavine, Fundamentals of Heat and Mass
703           Transfer, John Wiley and Sons, 2007. https://doi.org/10.1073/pnas.0703993104.

704    [40]  A. Marmur, Soft contact : measurement and interpretation of contact angles, Soft Matter. 2
705           (2006) 12–17. https://doi.org/10.1039/b514811c.

706    [41]  T. Young, An Essay on the Cohesion of Fluids, Philos. Trans. R. Soc. London. 95 (1805)
707           65–87.

708    [42]  R.N. Wenzel, Resistance of solid surfaces to wetting by water, Ind. Eng. Chem. 28 (1936)
709           988–994. https://doi.org/10.1021/ie50320a024.

710

711

712

713

714

715

716

Table 1 Data on roughness ratio, contact angle and interfacial tensions for various droplets and

their respective residues ($V_{fd}/V_{sd} =20$)

| Nanofluid/Hybrid Nanofluid | Roughness ratio $r$ | Apparent contact angle $\theta_a$ | Surface tension $\gamma_{lv}$ (mN/m) | Surface free energy $\gamma_{sv}$ (mN/m) | Solid-liquid interfacial tension $\gamma_{sl}$ (mN/m) |
|---|---|---|---|---|---|
| GNP | 1.351±0.143 | 8.57±0.89 | 72.433±0.121 | 56.075±0.274 | 3.071±0.363 |
| MR-1 0.1(Ag):0.9(GNP) | 1.379±0.095 | 9.49±0.13 | 68.752±0.130 | 56.671±0.193 | 7.523±0.174 |
| MR-2 0.3(Ag):0.7(GNP) | 1.305±0.157 | 26.06±0.06 | 64.558±0.226 | 55.138±0.327 | 10.724±0.298 |
| MR-3 0.5(Ag):0.5(GNP) | 1.216±0.073 | 24.41±0.32 | 67.812±0.478 | 60.074±0.217 | 9.312±0.267 |
| MR-4 0.7(Ag):0.3(GNP) | 1.238±0.126 | 41.44±0.07 | 63.288±0.172 | 57.468±0.194 | 19.173±0.138 |
| MR-5 0.9(Ag):0.1(GNP) | 1.191±0.087 | 52.19±3.08 | 59.546±0.170 | 52.291±0.329 | 21.652±0.327 |
| Ag | 1.194±0.138 | 142.64±0.52 | 58.927±0.209 | 43.962±0.285 | 83.163±0.243 |

719

720

721

722    Table 2 Surface properties of nanofluid/hybrid nanofluid residues

| Residue | Droplet Volume $V_{fd}$(µl) | Average Roughness $R_a$(µm) | Mean Feret Diameter $\emptyset_f$(µm) | Areal Porosity $a_p$(%) |
|---|---|---|---|---|
| GNP | 3 | 0.596±0.018 | 0.742±0.044 | 4.224±0.204 |
| | 15 | 1.399±0.260 | 0.751±0.132 | 23.362±0.632 |
| | 30 | 1.174±0.159 | 0.703±0.073 | 24.028±1.145 |
| | 60 | 1.960±0.161 | 0.740±0.059 | 24.483±0.655 |
| MR-1 | 3 | 0.626±0.094 | 0.255±0.006 | 17.157±0.846 |
| | 15 | 1.142±0.228 | 0.517±0.012 | 23.702±0.816 |
| | 30 | 1.362±0.223 | 0.780±0.033 | 25.826±0.589 |
| | 60 | 2.310±0.212 | 0.674±0.005 | 29.017±1.817 |
| MR-2 | 3 | 0.977±0.152 | 0.736±0.015 | 18.694±1.445 |
| | 15 | 1.510±0.158 | 0.796±0.006 | 19.388±0.949 |
| | 30 | 1.747±0.190 | 0.687±0.078 | 20.034±1.243 |
| | 60 | 1.826±0.202 | 0.618±0.027 | 23.469±0.139 |
| MR-3 | 3 | 0.824±0.099 | 0.695±0.023 | 14.299±0.260 |
| | 15 | 1.500±0.176 | 0.786±0.052 | 19.352±0.870 |
| | 30 | 1.792±0.231 | 0.753±0.101 | 21.066±2.226 |
| | 60 | 1.816±0.240 | 1.026±0.135 | 26.854±1.549 |
| MR-4 | 3 | 0.376±0.100 | 0.745±0.043 | 16.193±0.860 |
| | 15 | 1.299±0.157 | 0.722±0.021 | 18.918±1.761 |
| | 30 | 1.688±0.197 | 0.756±0.019 | 20.404±1.834 |
| | 60 | 1.606±0.201 | 0.711±0.022 | 21.006±0.886 |
| MR-5 | 3 | 0.322±0.035 | 0.408±0.008 | 7.651±0.666 |
| | 15 | 1.303±0.029 | 0.542±0.018 | 16.467±0.601 |
| | 30 | 1.574±0.141 | 0.543±0.024 | 16.841±0.067 |
| | 60 | 1.604±0.071 | 0.576±0.022 | 17.010±0.394 |
| Ag | 3 | 0.127±0.028 | 0.344±0.017 | 7.188±0.220 |
| | 15 | 1.038±0.014 | 0.385±0.048 | 7.674±0.497 |
| | 30 | 0.598±0.016 | 0.338±0.017 | 8.240±0.419 |
| | 60 | 0.914±0.071 | 0.390±0.004 | 8.814±0.571 |

723

724

725

726                                         (a)



727
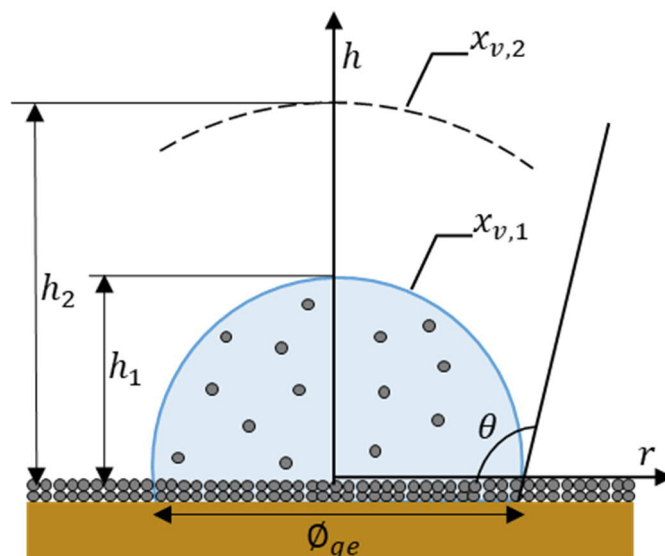
728                                         (b)
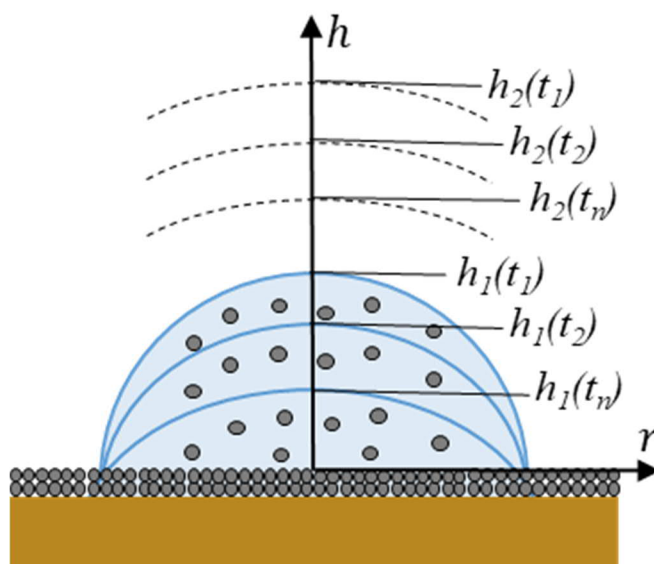
Fig. 1 (a) Ag-GNP nanofluid/hybrid nanofluid droplet evaporation over its residue surface. The suspended nanoparticles (grey balls) in the droplet settle down to form a porous residue surface during the evaporation process, (b) Schematics showing the evaporation of a pinned droplet with varying contact angle over its residue surface over a period of time $t_n$
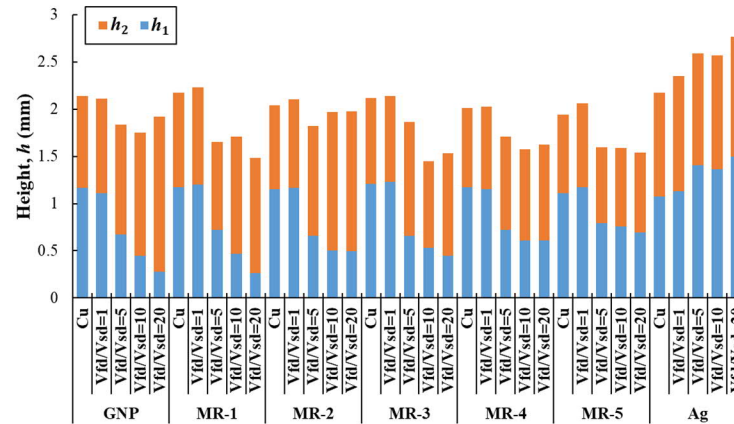
733

734

(a)



(b)



(c)
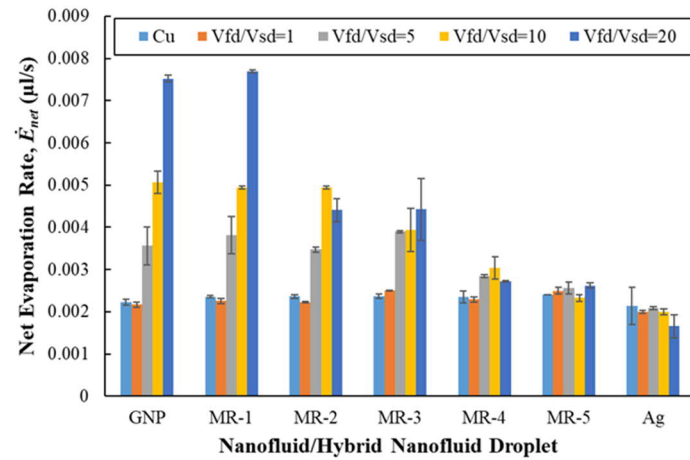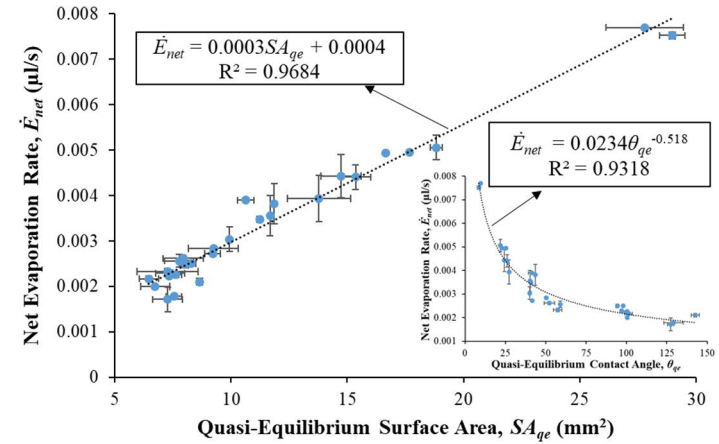
Fig. 2 (a) Net evaporation rate of Ag-GNP nanofluid/hybrid nanofluid droplets over Cu surface and their respective residue surfaces, (b) Net evaporation rate dependence on quasi-equilibrium surface area, (c) Variation of droplet height ($h_1$) and *VES* height ($h_2$) for Ag-GNP nanofluid/hybrid nanofluid droplets sitting on Cu surface and their respective residue surfaces at quasi-equilibrium state.

(a)

(b)

(c)

(d)

(e)

(f)

(g)
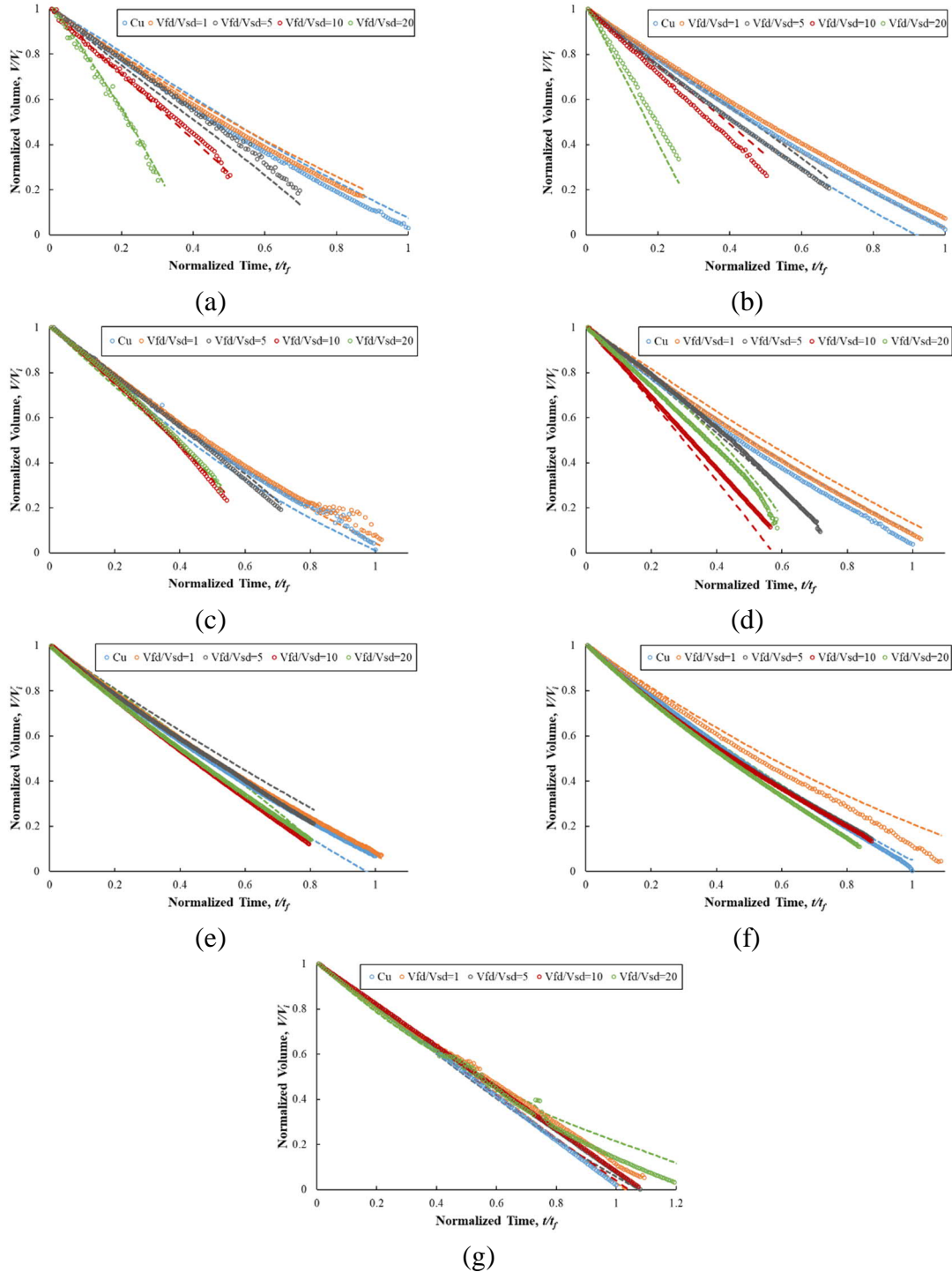
Fig. 3 Droplet volume variation with time for (a) GNP nanofluid, (b) MR-1 hybrid nanofluid, (c) MR-2 hybrid nanofluid, (d) MR-3 hybrid nanofluid, (e) MR-4 hybrid nanofluid, (f) MR-5 hybrid nanofluid and (g) Ag nanofluid droplets on Cu surface and respective residue surfaces. Unfilled markers represent the experimental data while dashed lines represent the theoretical result from equation (4).

(a)

(b)

(c)

(d)
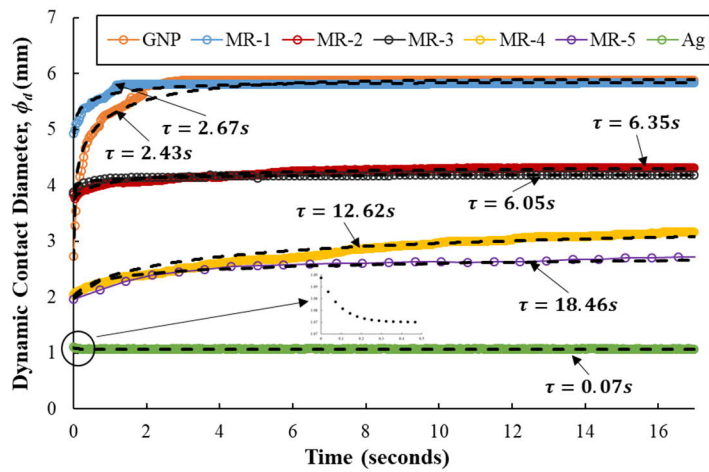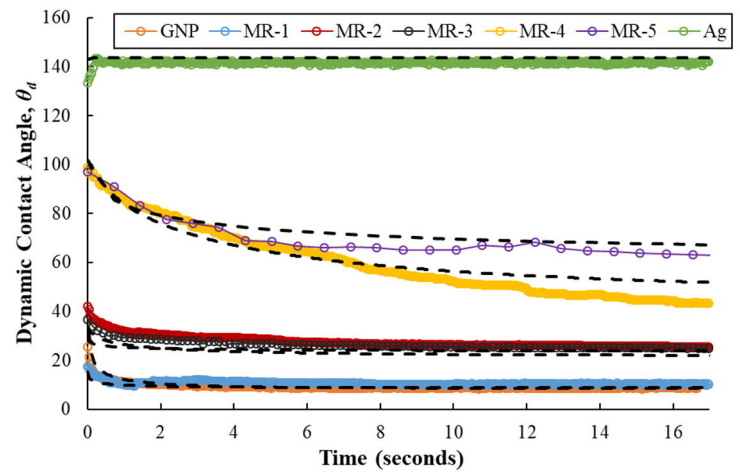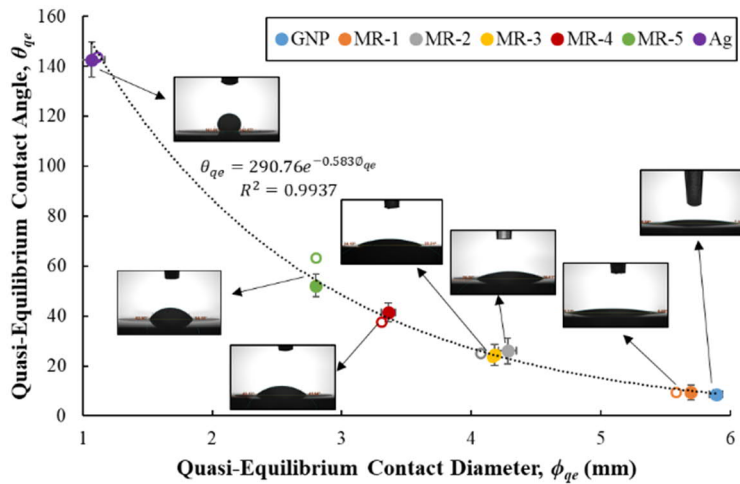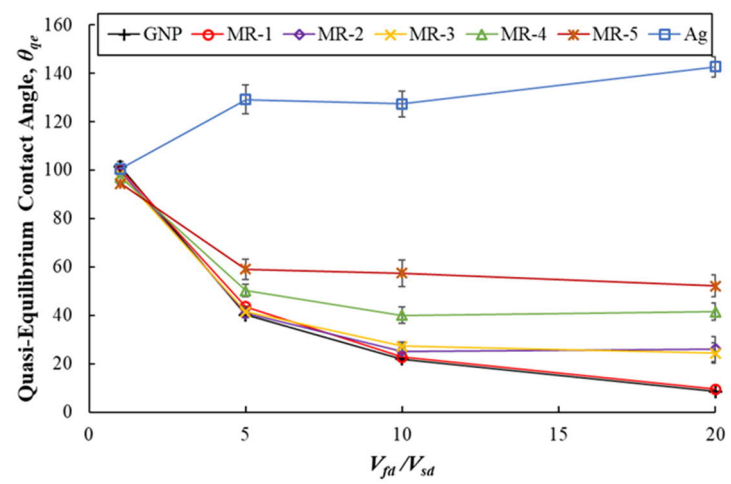
Fig. 4 Nanofluid/hybrid nanofluid droplet spreading over respective residue surfaces showing (a) dynamic contact diameter and (b) dynamic contact angle with time for $V_{fd}/V_{sd}$=20. Colored markers represent experimental data and dashed lines represent theoretical result, (c) Experimental (filled markers) and theoretical (unfilled markers) contact angle and contact diameter at quasi-equilibrium state for nanofluid/hybrid nanofluid droplets at $V_{fd}/V_{sd}$=20, (d) Quasi-equilibrium contact angle variation with factor $V_{fd}/V_{sd}$.
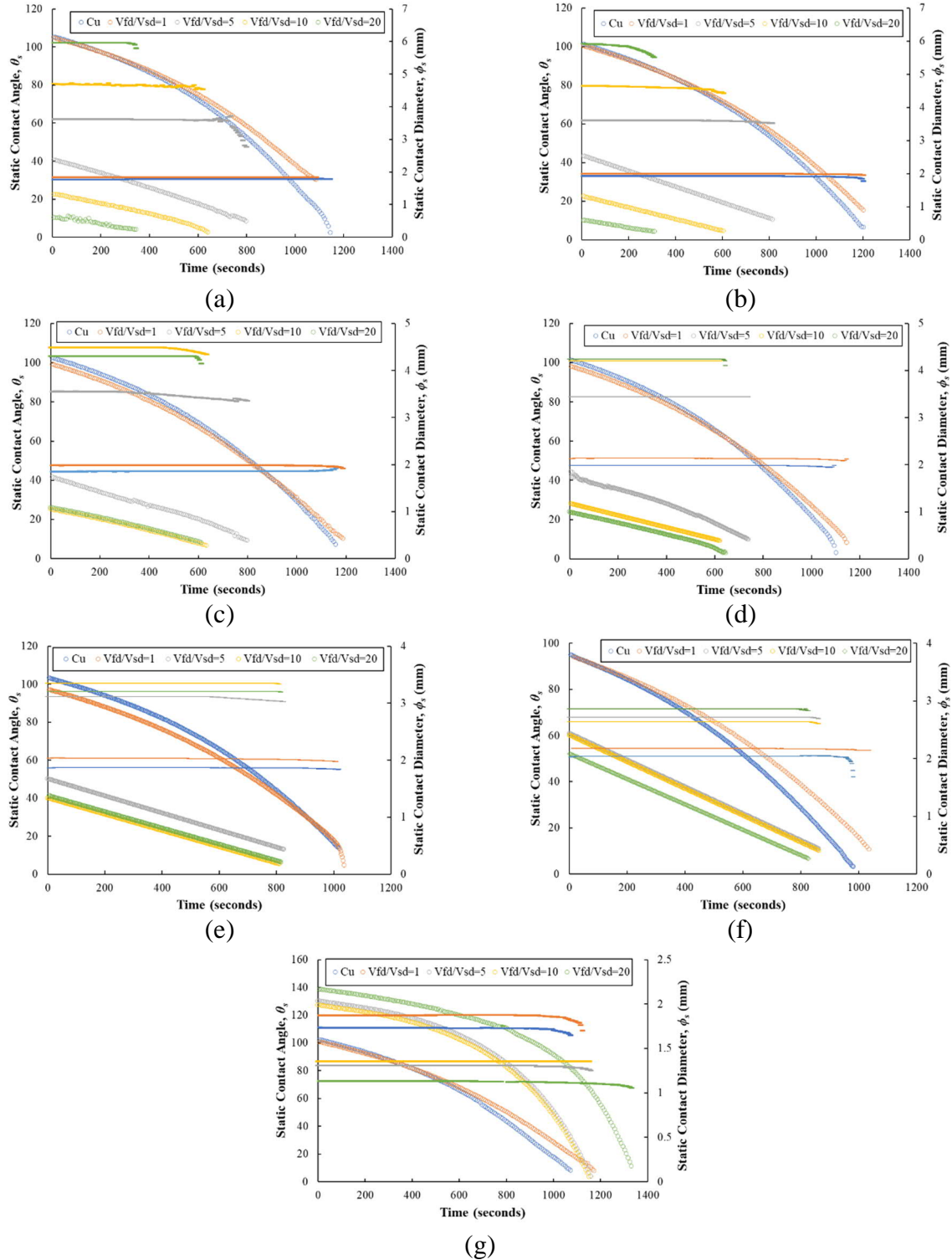
Fig. 5 Static contact angle (unfilled circles) and contact diameter (dashed markers) variation with time during evaporation for (a) GNP nanofluid, (b) MR-1 hybrid nanofluid, (c) MR-2 hybrid nanofluid, (d) MR-3 hybrid nanofluid, (e) MR-4 hybrid nanofluid, (f) MR-5 hybrid nanofluid and (g) Ag nanofluid droplets.

751

752

753

754

755

756
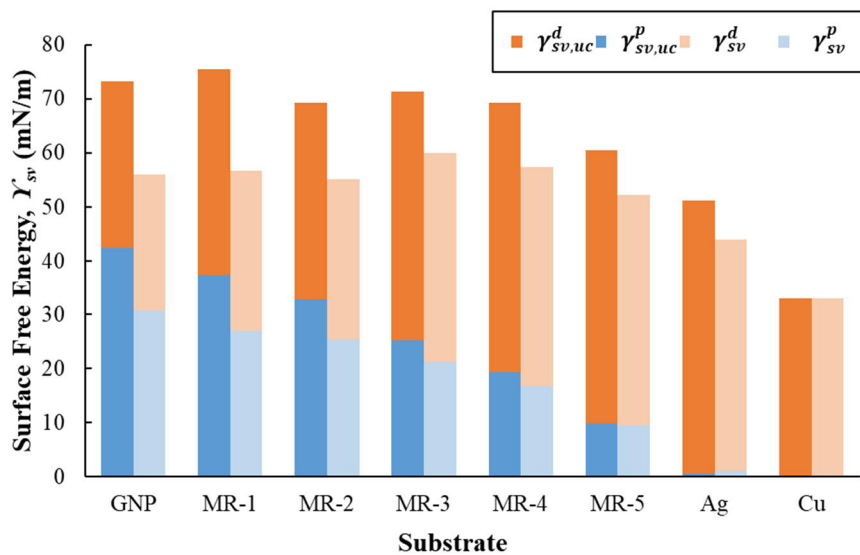


Fig. 6 Surface free energy of Cu surface and Ag-GNP nanofluid/hybrid nanofluid droplet residue surfaces. Superscripts *p* and *d* represent the polar and dispersive components, while subscript *sv,uc* represent the roughness uncorrected surface free energy.

761

762

763

**Supplementary Material**

765

## A. Empirical Model for term $dx_v/dh$

767    An empirical model is developed for term $dx_v/dh$ pertaining to equation (11) of our main article

768    as a function of the static contact angle ($\theta_s$), mixing ratio ($MR$) and droplet volume ratio $V_{fd}/V_{sd}$.

769    The values for $MR$ used in our empirical model are 0, 0.1, 0.3, 0.5, 0.7, 0.9 and 1 for GNP, MR-1,

770    MR-2, MR-3, MR-4, MR-5 and Ag respectively. The values used for $V_{fd}/V_{sd}$ are 0, 1, 5, 10 and

771    20, where the value 0 corresponds to the droplet resting on a pure copper surface. The developed

772    empirical model contains higher order polynomial terms to fit a large amount of experimental data

773    (6332 data points) and due to the variability in $dx_v/dh$ values with changing $\theta_s$, $MR$ and $V_{fd}/V_{sd}$

774    values. For this reason, higher order interaction terms are also included in our empirical model to

775    increase the model accuracy. The redundant terms with low coefficient values and p value>0.05

776    were removed from the model to obtain a non-hierarchical model while it was ascertained that the

777    model accuracy is not compromised. However, some terms with p value<0.05, despite having very

778    low coefficient values, were kept in the model as their removal affected the model accuracy. The

779    proposed empirical model is given as:

781
$$\frac{dx_v}{dh} = a + \sum_{i=1}^{n} \Bigg[ b_i \left(\frac{V_{fd}}{V_{sd}}\right)^i + c_i(MR)^i + d_i(\theta)^i$$

782
$$+ \sum_{j=1}^{k} \left( e_{ij}(MR)^i \left(\frac{V_{fd}}{V_{sd}}\right)^j + f_{ij}(\theta)^i \left(\frac{V_{fd}}{V_{sd}}\right)^j + g_{ij}(\theta)^i(MR)^j + \sum_{m=1}^{p} h_{ijm}\theta^i MR^j \left(\frac{V_{fd}}{V_{sd}}\right)^m \right) \Bigg]$$

780
$$(A.1)$$

783    The coefficient of determination ($R^2$), the adjusted coefficient of determination ($R^2$-adj) and the

784    predicted coefficient of determination ($R^2$-pred) of this model is 94.14%, 94.10% and 93.98%

785    respectively. This suggests that the proposed high fidelity model can be extrapolated to predict

786    $dx_v/dh$ with high level of confidence. Table A.1 shows the coefficient values for all terms used

787    in our model. All coefficient values are used up to the 10 decimal places due to high sensitivity of

788    the proposed model as shown in Table A.1. The residual plots in Fig. A.1 (a) and (b) show that the

789    model fits the experimental data with high accuracy.

790

791

## B. Residue Morphology and Pore Size Distribution

The SEM micrographs of nanostructured residues, developed by evaporating 60 µl of Ag-GNP nanofluid/hybrid nanofluid droplets over the Cu substrate, are shown in Fig. B.1. It is observed that all residue surfaces have a porous structure, with varying pore size and shapes. Since GNP particles exist in the form of stacked sheets, the pores created by the deposition of GNP particles during the GNP nanofluid droplet evaporation are different in size and shape, as compared to the ones created by the spherical Ag nanoparticles during the Ag nanofluid droplet evaporation. It must also be noted that the residue formed by Ag nanofluid droplet is not uniform (as shown in Fig. B.1 (g)), which indicates possible agglomeration of spherical Ag nanoparticles due to the increased particle concentration during the droplet evaporation process, thus resulting in non-uniform deposition with some large clustered Ag particles in the residue.

Fig. B.2 shows the pore size distribution for various residue sizes (from $V_{fd}$ =3 µl to $V_{fd}$ =60 µl) of Ag-GNP nanofluid/hybrid nanofluid droplets. It is observed that a large proportion of pores exist in sub-micron scale, while only a few are above 1 µm size, for all droplet residues. A large proportion of sub-micron pores are even below 0.5 µm in size, as shown in Fig. B.2. It is further noticed that the number of pores above 1 µm size increases, as the residue size is increased (from $V_{fd}$ =3 µl to $V_{fd}$ =60 µl).

Table A.1 Coefficient values for different terms used in equation (A.1)

| Coefficient | Value | Coefficient | Value | Coefficient | Value | Coefficient | Value |
|---|---|---|---|---|---|---|---|
| $a$ | 0.0317573471 | $c_4$ | 2.5615539109 | $f_{23}$ | - | $f_{24}$ | - |
| $b_1$ | -0.0025278216 | $d_4$ | - | $g_{23}$ | - | $g_{24}$ | -0.0000023049 |
| $c_1$ | 0.0151831037 | $e_{13}$ | 0.0013147213 | $e_{32}$ | 0.0086316105 | $e_{33}$ | 0.0003042131 |
| $d_1$ | - | $f_{13}$ | 0.0000703085 | $f_{32}$ | - | $f_{33}$ | - |
| $b_2$ | 0.0006233281 | $g_{13}$ | -0.0278015847 | $g_{32}$ | - | $g_{33}$ | - |
| $c_2$ | -0.2498280817 | $e_{22}$ | 0.0190898913 | $e_{41}$ | - | $e_{42}$ | -0.0105948253 |
| $d_2$ | - | $f_{22}$ | - | $f_{41}$ | - | $f_{42}$ | - |
| $e_{11}$ | 0.0399835796 | $g_{22}$ | 0.0000033475 | $g_{41}$ | - | $g_{42}$ | - |
| $f_{11}$ | - | $e_{31}$ | -0.1472236199 | $h_{113}$ | - | $e_{51}$ | 0.1057676989 |
| $g_{11}$ | - | $f_{31}$ | -0.0000000072 | $h_{122}$ | -0.0000855998 | $f_{51}$ | - |
| $b_3$ | -0.0000732252 | $g_{31}$ | - | $h_{131}$ | 0.0012069307 | $g_{51}$ | - |
| $c_3$ | - | $h_{112}$ | 0.0000095663 | $h_{212}$ | - | $h_{114}$ | 0.0000000303 |
| $d_3$ | -0.0000000149 | $h_{121}$ | 0.0004073719 | $h_{221}$ | - | $h_{123}$ | - |
| $e_{12}$ | -0.0139787722 | $h_{211}$ | -0.0000035763 | $h_{311}$ | - | $h_{132}$ | 0.0000549784 |
| $f_{12}$ | -0.0002364804 | $b_5$ | - | $b_6$ | - | $h_{141}$ | -0.0012308752 |
| $g_{12}$ | 0.0061591758 | $c_5$ | -4.4061392885 | $c_6$ | 2.0923883089 | $h_{213}$ | -0.0000000014 |
| $e_{21}$ | - | $d_5$ | - | $d_6$ | - | $h_{222}$ | 0.0000000696 |
| $f_{21}$ | 0.0000026388 | $e_{14}$ | -0.0000349963 | $e_{15}$ | - | $h_{231}$ | - |
| $g_{21}$ | - | $f_{14}$ | -0.0000065444 | $f_{15}$ | 0.0000001805 | $h_{312}$ | -0.0000000001 |
| $h_{111}$ | -0.0001361987 | $g_{14}$ | 0.0386800317 | $g_{15}$ | -0.0172854142 | $h_{321}$ | 0.0000000106 |
| $b_4$ | 0.0000023456 | $e_{23}$ | -0.0019666568 | $e_{24}$ | 0.0000449429 | $h_{411}$ | - |

(a)



(b)
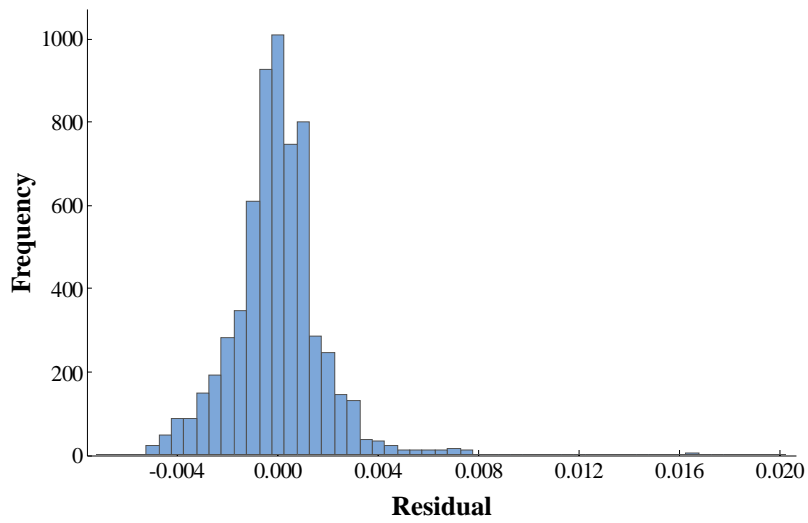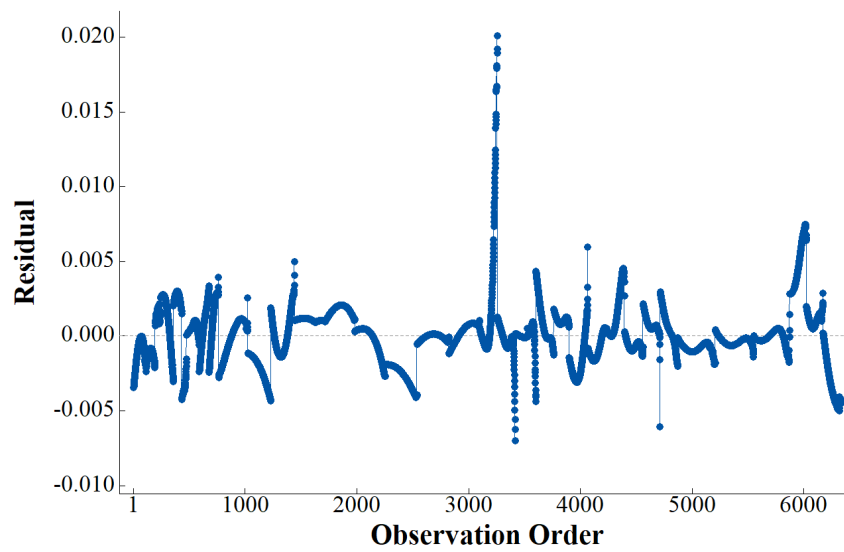
Fig. A.1 (a) Histogram of residuals and (b) Residual versus order plot pertaining to the empirical equation (A.1)

827

828



(a)　　　　　　　　　(b)　　　　　　　　　(c)

(d)　　　　　　　　　(e)　　　　　　　　　(f)

(g)
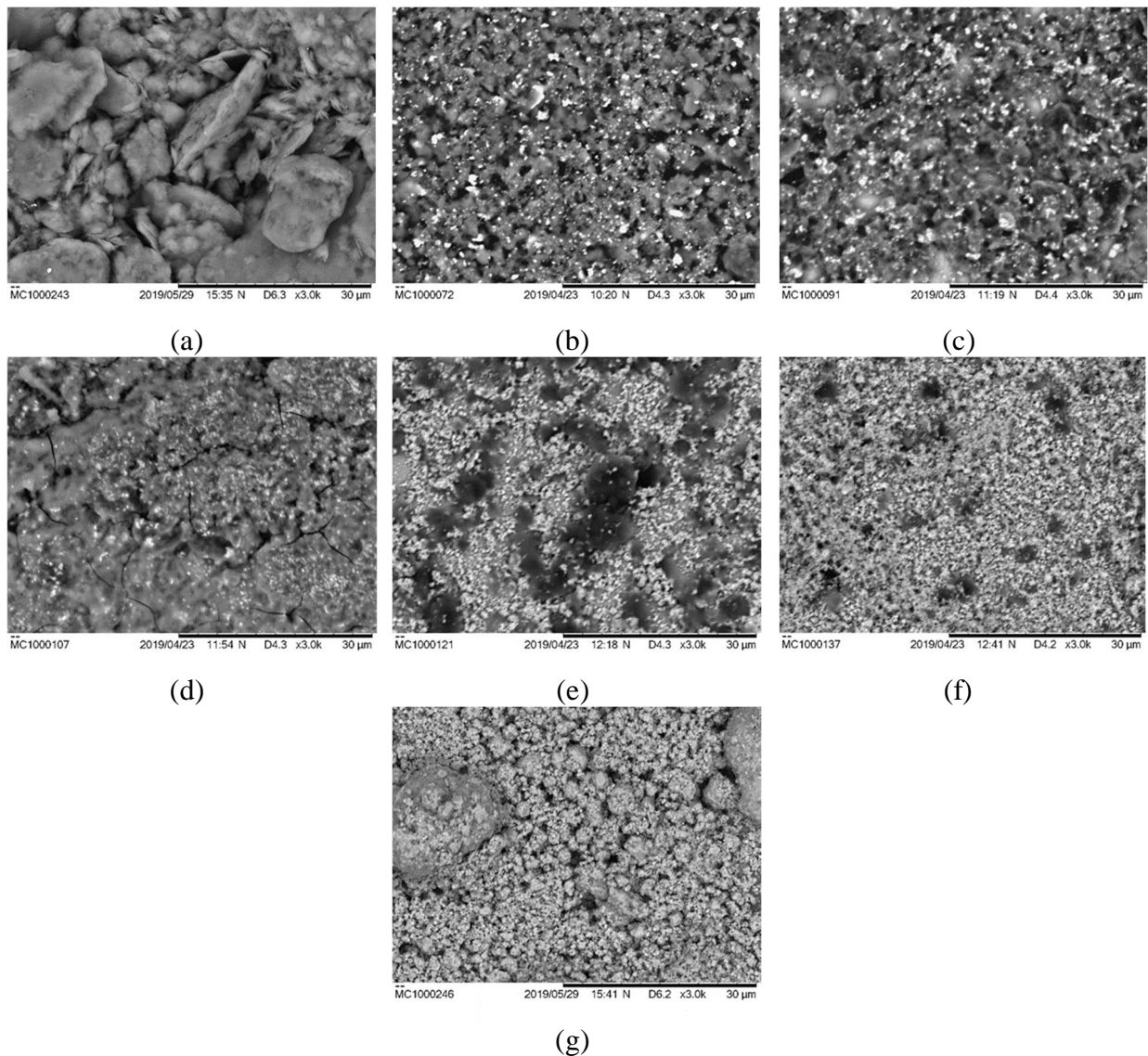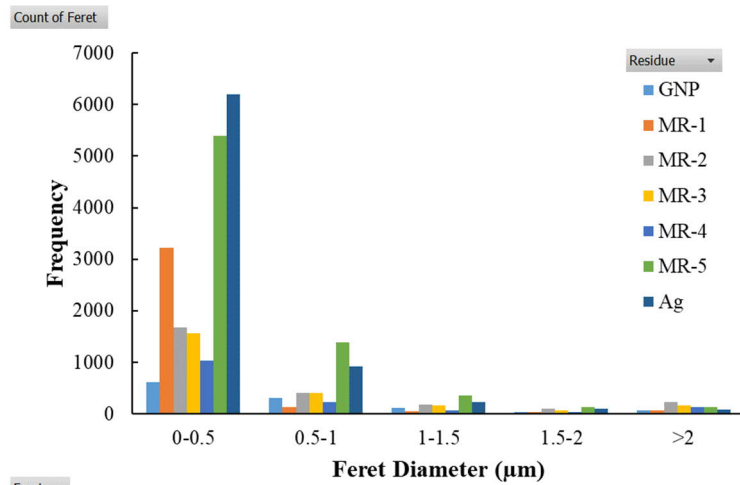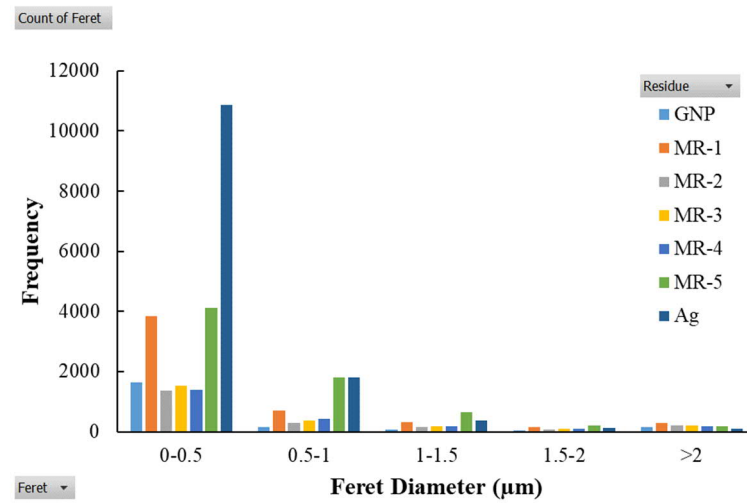
829　　Fig. B.1 SEM micrographs of residues developed from 60µl volume of (a) GNP nanofluid, (b)

830　MR-1 hybrid nanofluid, (c) MR-2 hybrid nanofluid, (d) MR-3 hybrid nanofluid, (e) MR-4 hybrid

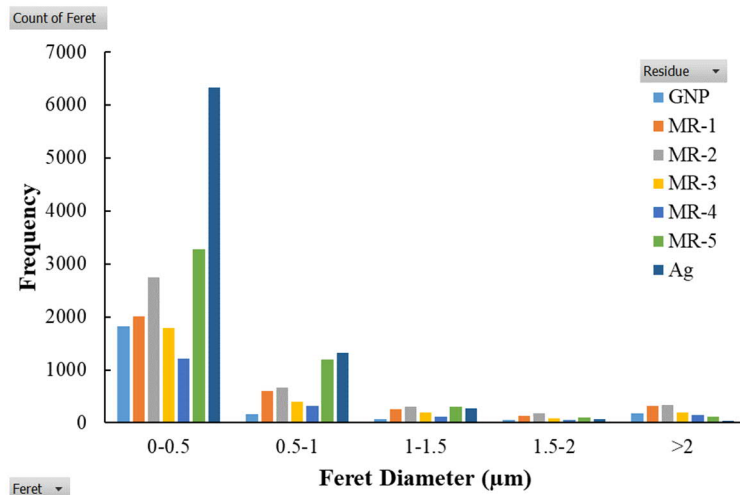831　　　　nanofluid, (f) MR-5 hybrid nanofluid and (g) Ag nanofluid droplets on Cu substrate.
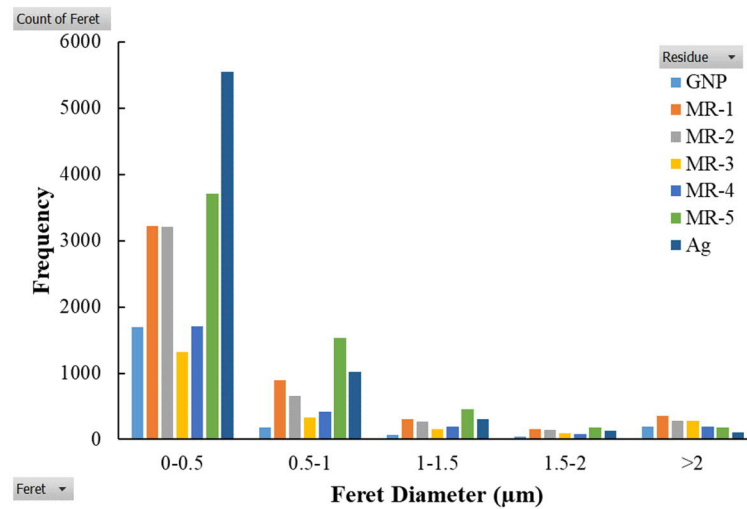
832

Fig. B.2 Pore size distribution for various mixing ratios of Ag-GNP hybrid nanofluid droplet residue corresponding to (a)$V_{fd}$ = 3µl, (b) $V_{fd}$ = 15µl, (c)$V_{fd}$ = 30 µl and (d)$V_{fd}$ = 60 µl.